Acta metall. Vol. 34, No. 5, pp. 761–800, 1986
Printed in Great Britain.

0001-6160/86 $3.00 + 0.00

OVERVIEW NO. 48

TOUGHENING OF BRITTLE SOLIDS BY MARTENSITIC TRANSFORMATIONS

A. G. EVANS† and R. M. CANNON

Materials and Molecular Research Division, Lawrence Berkeley Laboratory, and Department of Materials Science and Mineral Engineering, University of California, Berkeley, CA 94720, U.S.A.

(*Received* 9 *April* 1985)

CONTENTS

Abstract—A comprehensive review of toughening mechanisms in transformable brittle solids is presented. Primary emphasis is given to transformation toughening, although microcrack and deflection toughening are also considered. Models of toughness are developed using concepts from applied mechanics, but within the context of the thermodynamics and kinetics of the transformation process. The predictions of the models are compared with experimental data for various ZrO_2 containing ceramic alloys. It is concluded that the predominant toughening mechanism depends on the alloy composition and microstructure; dilatational transformation toughening with shear modifications dominates in partially stabilized zirconia; uniaxial transformation and microcrack mechanisms prevail in zirconia toughened alumina; transformation toughening with partial reversibility predominates in tetragonal zirconia polycrystals.

Résumé—Nous présentons une revue complète des mécanismes de durcissement dans les solids fragiles transformables. Nous insistons surtout sur le durcissement par transformation, bien que nous considérions également le durcissement par microfissure et par déviation. Nous développons des modèles de durcissement à l'aide de concepts de la mécanique appliquée, mais dans le contexte de la thermodynamique et de la cinétique de la transformation. Nous comparons les prévisions du modèle avec les résultats expérimentaux dans diverses céramiques alliées contenant du ZrO_2. Nous en concluons que le mécanisme d'endurcissement prépondérant dépend de la composition et de la microstructure de l'alliage; un durcissement de transformation de dilatation avec des modifications de cisaillement domine dans la zircone partiellement stabilisée; la transformation uniaxiale et les mécanismes de microfissuration prévalent dans l'alumine durcie à la zircone; le durcissement de transformation avec une réversibilité partielle prédomine dans les polycristaux de zircone quadratique.

†Present address: College of Engineering, University of California, Santa Barbara, CA 93106, U.S.A.

Zusammenfassung—Die Arbeit gibt einen umfassenden überlick über die Verstärkungsmechanismen in umwandlungsgeeigneten spröden Keramiken. Der Schwerpunkt liegt auf der Umwandlungsverstärkung, obwohl auch die Verstärkung durch Mikrorisse und Umbiegung berücksichtigt wird. Mit Konzepten aus der angewandten Mechanik, jedoch im Rahmen von Thermodynamik und Kinetik der Umwandlungsprozesse werden Verstärkungsmodelle entwickelt. Die Voraussagen dieser Modelle werden mit experimentellen Ergebnissen verglichen, die an verschiedenen ZrO_2-haltigen keramischen Legierungen erhalten worden sind. Daraus ergibt sich, daß der vorweigende Verstärkungsmechanismus abhängt von Legierungszusammensetzung und Mikrostruktur. Die Verstärkung durch Dilatationsumwandlung mit Modifikation durch Scherung überwiegt im teilstabilisierten Zirkonoxid. Mechanismen mit einachsiger Umwandlung und Rißbildung liegen im Zirkonoxid-haltigen Aluminiumoxid vor. Die Umwandlungsverstärkung mit teilweiser Reversibilität überwiegt in Polykristallen aus tetragonalem Zirkonoxid.

1. INTRODUCTION

During the last decade, it has been unequivocally established that stress induced martensite transformations can substantially enhance the fracture toughness of, otherwise, brittle solids [1–7]. The effect has been most extensively investigated in ZrO_2 and in various matrices with a ZrO_2 second phase. In this system, the transformation entails a change from the tetragonal to the monoclinic phase. However, similar transformations occur in HfO_2 and possibly quartz and cordierite. Order of magnitude increases in toughness (K_c) have been reported in selected instances. Commensurate increases in fracture strength often accompany this mode of toughening [3, 5, 8] (Fig. 1). Such large effects are unprecedented in material systems incapable of crack tip blunting. The scientific bases underlying this phenomenon have progressed at a similarly remarkable pace, due to broad ranging contributions from ceramic science and applied mechanics [9, 10]. The associated scientific principles are examined in the present article.

The fundamental basis for comprehending the toughening phenomenon resides in the thermodynamics and associated kinetics of the stress induced transformation. The basic thermodynamics, plus consideration of the pertinent nucleation and growth processes, permit descriptions of expected trends in the stress–strain characteristics of material containing various types of transforming particles. The ensuing trends in stress–strain behavior allow constitutive laws (that determine the stress and displacement fields near crack tips) to be derived. Such understanding is necessitated by an inability to independently access stress–strain information from macroscopic specimens, because fracture intervenes before appreciable inelastic strains develop [11, 12]. The constitutive laws lead directly to descriptions of crack tip fields which, in turn, define the levels of transformation toughening. The pertinent energetics and kinetics and the resultant transformation toughening are given explicit consideration in this article. Alternate, independent ways of considering the toughening in terms of shielding by crack tip closure forces or energy dissipation from transformation hysteresis are presented and shown to provide equivalent predictions.

In some material systems, transformation induces microcracking. The associated microcrack induced strains can be an alternative source of toughness. Furthermore, cracks may be deflected by the residual fields associated with the transformed particles. The deflection process may also contribute to the toughness. Microcrack and deflection toughening are thus alternative or additional toughening mechanisms in transformable, brittle solids and preliminary models are presented for each.

Finally, some experimental data on the toughness of various material systems are summarised and compared with the available models, as required to provide a rationale for the observed trends.

2. MATERIALS AND TRANSFORMATIONS

The most comprehensive experimental observations amenable to comparison with the predicted behavior have been obtained on partially stabilized ZrO_2 (PSZ), particularly MgO/PSZ. Appreciable information has also been gained on certain ZrO_2 toughened aluminas (ZTA). Primary emphasis is placed on these materials. However, the behavior of tetragonal ZrO_2 polycrystals (TZP) is also given cursory consideration.

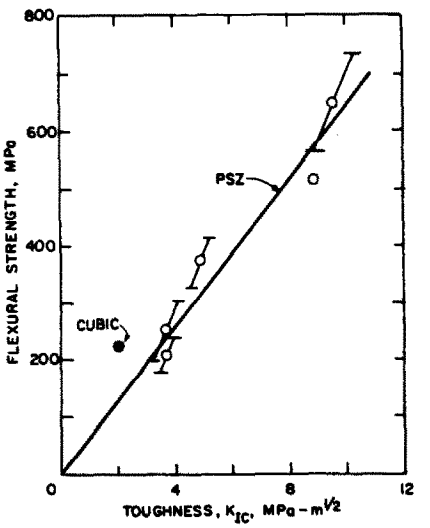

Fig. 1. Flexural strength plotted against K_c for CaO/PSZ materials after various heat treatments [1].

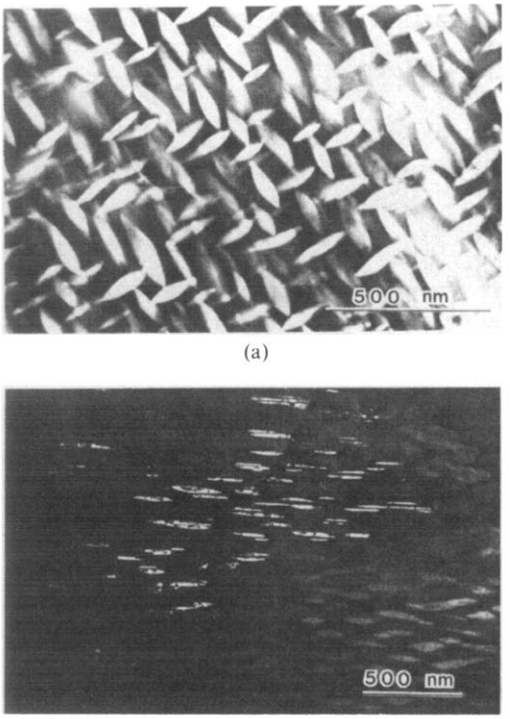

Fig. 2. Transmission electron micrograph of MgO/PSZ with: (a) lens shaped tetragonal precipitates; (b) precipitates transformed by the passage of a crack (courtesy A. H. Heuer).

The PSZ materials consist of relatively large grains of cubic ZrO_2 containing coherent, submicron sized precipitates of tetragonal ZrO_2. The precipitates in MgO/PSZ are lens shaped (aspect ratio 5:1) [Fig. 2(a)], and the axes of the precipitates lie along the cube axes of the matrix [7, 13, 14]. In contrast, the precipitates in CaO/PSZ are nearly equiaxed [7]. Typically volume fractions, f, of 0.3 to 0.5 can be obtained [6]. Stress induced transformation of the tetragonal ZrO_2 to the monoclinic phase generally induces incoherency and results in the formation of a small number of parallel twins. In MgO/PSZ the twin plane normal generally coincides with the minor axis of the precipitate Fig. 2b [7, 13, 15]. The transformation also induces a volume increase, ε_{ii}^{T}, of about 4–6% which may be affected by solute [7, 16]. The shear strains associated with individual twins are much larger (of order 14%) [17], but due to the appearance of several twins in each precipitate, the long range shear strains are usually considered to be relatively small (viz. a few percent) [16]. Crack propagation in these materials is primarily transgranular, unless excessive grain boundary precipitates have developed during heat treatment [1, 18]. The highest toughnesses measured for PSZ systems are [19] $K_c \approx 18$ MPa-m$^{1/2}$.

The ZTA materials are fabricated by co-sintering fine Al_2O_3 and ZrO_2 powders [4, 5]. This procedure results in an essentially isolated tetragonal ZrO_2 phase contained largely at three and four grain junctions. Such particles are thus strongly angular [Fig. 3(a)], as expected from dihedral angle considerations [20]. When the sintering conditions allow appreciable grain growth, ellipsoidal intragranular particles are also present [Fig. 3(a)], and can be prevalent at low ZrO_2 concentrations (e.g. <10 vol.%) [20, 21]. The angular ZrO_2 particles at the grain junctions have been observed to transform more readily than the ellipsoidal intragranular particles [20, 22], suggestive of an influence of corners on the nucleation process. The orientations of the ZrO_2 particles in ZTA are usually random. After transformation, submicron particles typically exhibit a single set of parallel twins [Fig. 3(b) and 3(c)]; these are often aligned relative to the tetragonal parent, although randomly oriented amongst particles

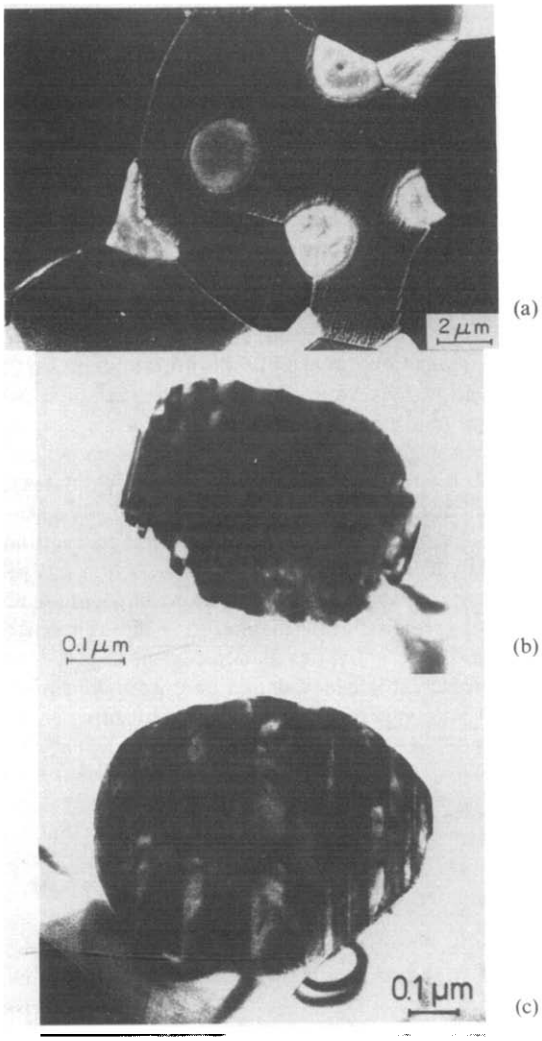

Fig. 3. Microstructures of ZTA materials: (a) scanning electron micrograph showing angular ZrO_2 particles at grain junctions and ellipsoidal, intragranular ZrO_2 particles (courtesy A. H. Heuer and M. Rühle); (b) TEM micrograph of a transformed, twinned ZrO_2 particle (courtesy W. M. Kriven and M. Rühle); (c) TEM micrograph of transformed, twinned ZrO_2 particle wherein small additional twins reduce discontinuities at twin terminations (courtesy W. M. Kriven and M. Rühle).

[22, 23]. Larger particles develop more complex twinning, in ZTA as well as in PSZ [14, 23]. The ZTA materials are relatively tough (K_c up to 14 MPa-m$^{1/2}$) and can exhibit high strength (1–2 GPa or higher) [3–5, 24].

The TZP materials are fine grained polycrystals of tetragonal ZrO_2 partially stabilized with Y_2O_3 or CeO_2, and fabricated by sintering [25–27]. When transformation occurs in such materials, entire grains usually transform, typically with an appreciable number of twins in each grain [28]. A range of strengths and toughnesses have been achieved. The highest strengths are in the 1–2 GPa range, but these strengths are not obtained on the materials with the highest toughness [12, 29], $K_c > 14$ MPa-m$^{1/2}$. A tentative framework for interpreting this behavior is presented in the following section.

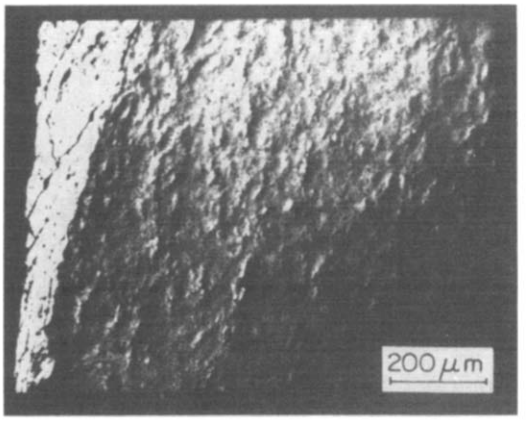

Fig. 5. Deformation markings and incipient shear bands observed on the tensile surface of a PSZ material (courtesy M. V. Swain).

3. THE TOUGHENING AND STRENGTHENING PHENOMENA

Broad ranging variations in the strength and toughness of transformation toughened ZrO_2 systems have been reported. A comprehensive framework for interpreting these trends has not been fully established. A tentative rationalization is presented here, as a basis for the subsequent analytic developments. The suggested behavior invokes an analogy with the mechanical properties of steels in the ductile-to-brittle transition range [30]. This notion follows from a proposal by Swain [12], based on a set of recent strength and toughness observations.

When transformation toughening operates, it is now well established that the toughness, K_c, increases as the critical stress at which the transformation nucleates, σ_c, decreases (Fig. 4)—detailed relations between K_c and σ_c are developed in Section 6. Consequently, when fracture initiates at flaws (diameter a) that pre-exist in the material, the failure strength [31] ($\sigma_f \propto K_c a^{-1/2}$) varies as depicted in Fig. 4.

However, it is believed that another failure mechanism intervenes at small σ_c. Specifically, as the critical stress decreases, recent evidence obtained on unnotched specimens of highly toughened MgO/PSZ reveals that generalised, but microstructurally localized nonlinear deformation, manifest as incipient shear bands (Fig. 5), preceeds fracture [11, 12]. The onset of deformation is sometimes accompanied by measurable deviations from linearity. Similar effects occur in steels within the brittle to ductile transition range [30]. Furthermore, in steels, the inhomogeneity of the slip process causes microcracks to initiate at the yield strength. The microcracks rapidly become unstable and induce brittle failure. Consequently, the fracture strength scales with the yield strength. The behavior persists until slip becomes sufficiently homogeneous that unstable microcrack propagation is inhibited. A transition to ductile fracture then ensues. The concept of yield limited strength suggests that generalised shear band formation may also initiate fracture in ZrO_2 systems. In fact, it seems probable that, due to the inhomogeneity of the shear band deformation and the accompanying dilatation, microcrack nucleation will occur more readily at shear band terminations in ZrO_2 [32] than at slip band intersections in steels. Consequently, it is proposed that the failure strength at small σ_c is yield limited, causing the mechanism transition depicted in Fig. 4. A strength maximum, $\hat{\sigma}_f$, would then be expected in the brittle range (Fig. 4). The maximum occurs at a critical value of the yield strength, contingent upon the size of the dominant pre-existing flaws.

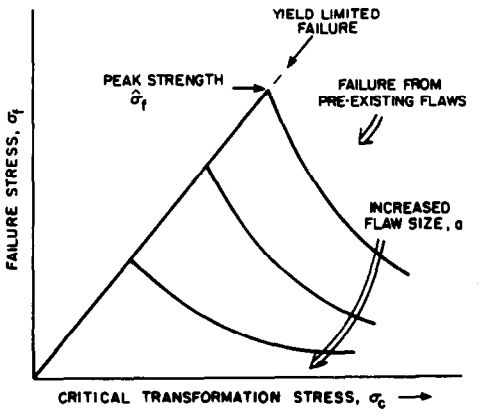

Fig. 4. A schematic illustrating a proposed relation between strength and toughness in ZrO_2 toughened material.

Finally, continuation of the analogy with steels would imply a transition to ductile fracture, when crack tip blunting occurs [33]. However, this transition is unlikely in ZrO_2 because the transformation provides limited plasticity [9, 10, 34] and the large, homogeneous deformations needed to achieve blunting are unavailable.

The preceding description of trends in strength and toughness is complicated in some instances by surface compression effects, associated with transformed sur-

face layers [1, 5]. Compressed surface layers formed by grinding inhibit the incidence of failure from near-surface flaws located within the compressed layer. (Failure from sub-surface flaws is clearly unaffected, or slightly enhanced.) The compressive residual stress, σ_R, in the layer can be extremely large. Specifically, the residual stress is given by

$$\sigma_R = E\varepsilon_{ii}^T f/3(1-\nu) \tag{3.1}$$

where E is Young's modulus, ν is Poisson's ratio, ε_{ii}^T is the total dilatational transformation strain and f is the volume fraction of transformed material in the layer. For typical ZrO_2 systems, equation (3.1) indicates residual stresses of order 1 GPa, consistent with X-ray measurements [35]. Such large stresses inhibit failure from flaws within the layer (despite the lower toughness associated with the transformed material). Substantial strength increases are thus observed in situations where the maximum tensile stresses occur at the surface (e.g. thermal shock and bending). However, it is noted that residual compressive effects should only obtain when pre-existing flaws control strength (at large σ_c), and should be of no significance when yield limited behavior develops (at small σ_c).

4. TRANSFORMATION THERMODYNAMICS AND KINETICS

4.1. General considerations

A martensite transformation is accompanied by a net change in the Gibbs free energy, G, for each transformed volume element, δV, given in general by [24, 36–39]†

$$\frac{\delta G}{\delta V} = -\Delta G_0 - (\sigma_{ij} + \sigma_{ij}^I/2)\varepsilon_{ij}^T + \frac{\delta \Delta\gamma A}{\delta V} + \frac{\delta \gamma_t A_t}{\delta V} \tag{4.1}$$

where ΔG_0 is the chemical free energy per unit volume which, when martensite is the low temperature phase, is given approximately by

$$\Delta G_0 = \Delta S\,(T_0 - T) \tag{4.2}$$

with ΔS as the entropy of the reverse transformation and T_0 the stress free equilibrium transformation temperature. The quantity $\sigma_{ij}\varepsilon_{ij}^T$ is the interaction energy associated with the *prior stress*, σ_{ij}, acting on the transformed *element*, subject to the unconstrained transformation strain ε_{ij}^T [37]. The stress in the transformed product, σ_{ij}^I, depends both on the element shape and on the transformation strain. The energy $\Delta\gamma$ is the excess surface energy for the monoclinic–tetragonal interface (or, in the latter stage of transformation, the energy difference between a product–matrix interface and a parent–matrix interface). The energies of twin, or other internal, boundaries are represented by γ_t.

†Subscript summation notation is utilized throughout.

The free energy change exhibits a relatively simple form when the transformation is purely dilational. Then, $\bar{\sigma}^I = \sigma_{ii}^I/3$ determines the energy and is shape independent; it is given by [37]

$$\bar{\sigma}^I = -B\varepsilon_{ii}^T(1-\alpha) \tag{4.3}$$

where $\alpha = (1+\nu)/3(1-\nu)$ and B is the bulk modulus. However, martensitic transformations entail substantial shear contributions, whereupon important shape effects emerge [37]. Thus, the shape of a transforming region generally tends to evolve to minimize the Gibbs free energy change due to the transformation. Typically, martensite initially forms as individual thin plates or oblate spheroids, because σ_{ij}^I varies strongly with the aspect ratio [38]. Consequently, the resultant change in ΔG with the fractional volume transformed, X, characteristically exhibits the variation depicted in Fig. 6. The initial increase in ΔG at small X (and the associated maximum) constitute a nucleation barrier. Once this barrier has been surmounted, by application of thermal or mechanical energy, the transformation proceeds to the minimum. Additional transformation would then require a further increase in external energy. The details of these processes can be elucidated for several idealized cases, which identify the essential features of the transformation.

At the nucleation stage, it is probable that the martensite forms as an untwinned oblate spheroid [38]. For this geometry, the free energy change has the form ($a \gg h$)

$$\frac{\Delta G}{2\pi a^2 h} = -\Delta G_0 - \sigma_{ij}\varepsilon_{ij}^T + A_0 + A_1\left(\frac{h}{a}\right) + \gamma\left[\frac{1}{h} + \frac{2}{a}\right] \tag{4.4}$$

where

$$A_0 = 2(1+\nu)\mu\Delta^2/9(1-\nu) \tag{4.5}$$

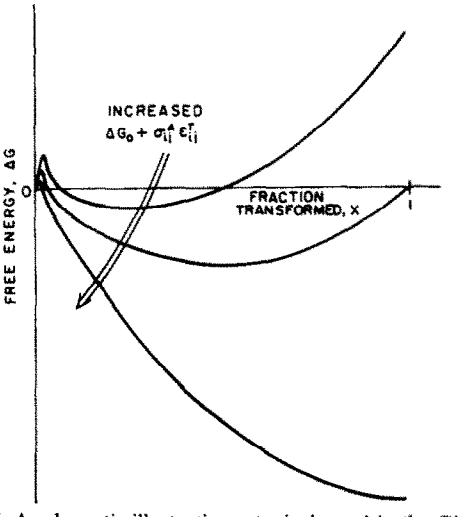

Fig. 6. A schematic illustrating a typical trend in the Gibbs free energy change, ΔG, with the volume fraction, X, of material transformed.

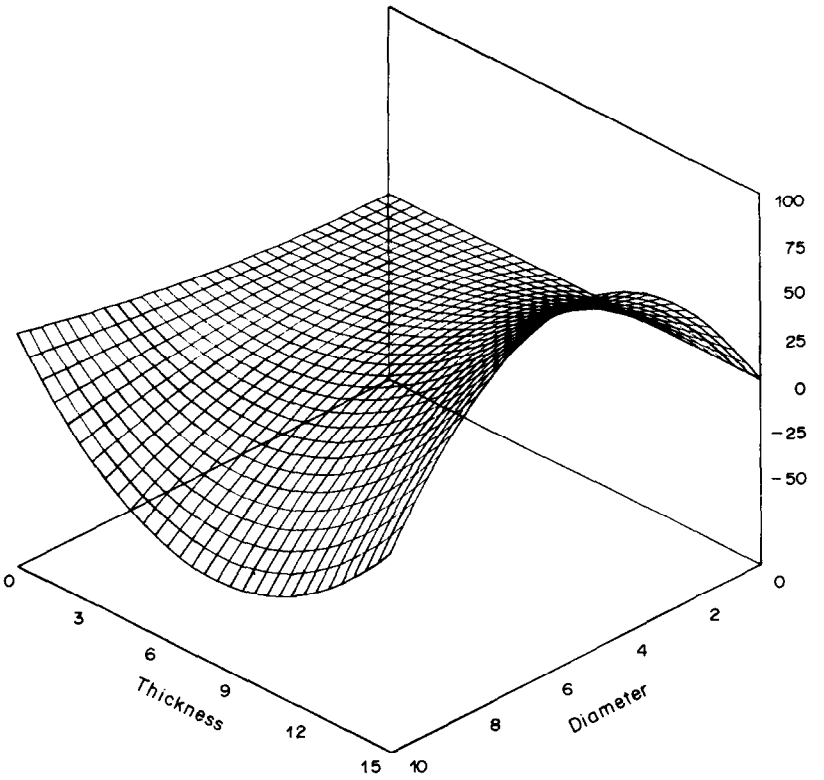

Fig. 7. Schematics of the free energy surface associated with the transformation indicating a saddle point and a low energy path.

and

$$A_1 = \pi\mu\left[\frac{(2-\nu)}{2(1-\nu)}\varepsilon_s^2 + \frac{\xi^2}{4(1-\nu)} + \frac{(1+\nu)}{3(1-\nu)}\xi\Delta\right] \tag{4.6}$$

with h and a representing the half-thickness and radius of the spheroid, respectively; ξ, Δ and ε_s are the transformation strains: specifically, $\xi + \Delta$ represents the net dilatation (such that the strain normal to the disc is $\xi + \Delta/3$, and the in-plane strains are $\Delta/3$), while ε_s is the out-of-plane shear strain. The trends in ΔG represented by equation (4.4) are plotted in Fig. 7 [39]. The saddle point in this diagram represents the homogeneous nucleation barrier. The associated free energy is

$$\Delta G^* = \frac{8\pi\gamma^3}{27G_n^2}\left[15 - \lambda + \frac{24}{\lambda} + \frac{8}{\lambda^2} + \frac{(\lambda^2+8\lambda+4)^{3/2}}{\lambda^2}\right] \tag{4.7}$$

where $G_n = (\Delta G_0 - A_0 + \sigma_{ij}\varepsilon_{ij}^T)$ and $\lambda = G_n/A_1$. Note that the surface energy is a dominant term during nucleation, and that ΔG^* can be reduced in the presence of applied (or residual) stresses, σ_{ij}. Beyond the saddle point, the radius, a, can increase without limit until a particle edge is encountered. Thickening can also occur until mechanical equilibrium is established.

Further growth usually involves the formation of twins. The details are complex and geometry sensitive. However, it is useful to note that the free energy of the ultimate twinned structure contains a strain energy term, U_t, associated with the short range strain at the twin terminations. For spherical particles with a parallel set of twins [36, 39]

$$U_t \simeq \frac{4(7-5\nu)}{15(1-\nu)}\frac{\mu\varepsilon_s}{(1+\eta)}V_p \tag{4.8}$$

where η is the number of twins. This strain energy term essentially superposes on the terms provided by the *net* transformation strain, ε_{ij}^T. Equivalent results for spheroidal particles have been obtained using finite element methods [40] (Fig. 8). Figure 8(a) shows the various contributions to the total free energy for the stress free case, and Fig. 8(b) shows the particle size dependence of the optimum number of twins.

When the twins are of uneven thickness and do not fully cancel the shear strain parallel to the twins a long range net shear strain, ε^{ns}, results. A useful approximation that describes the short and long range strain energy associated with this shear component is [39]

$$U_s \simeq \frac{2(7-5\nu)}{15(1-\nu)}\mu\varepsilon_s^2\left[\frac{2}{(1+\eta)} + \left(\frac{\varepsilon^{ns}}{\varepsilon_s}\right)^2\left(1 - \frac{2}{1+\eta}\right)\right]V_p. \tag{4.9}$$

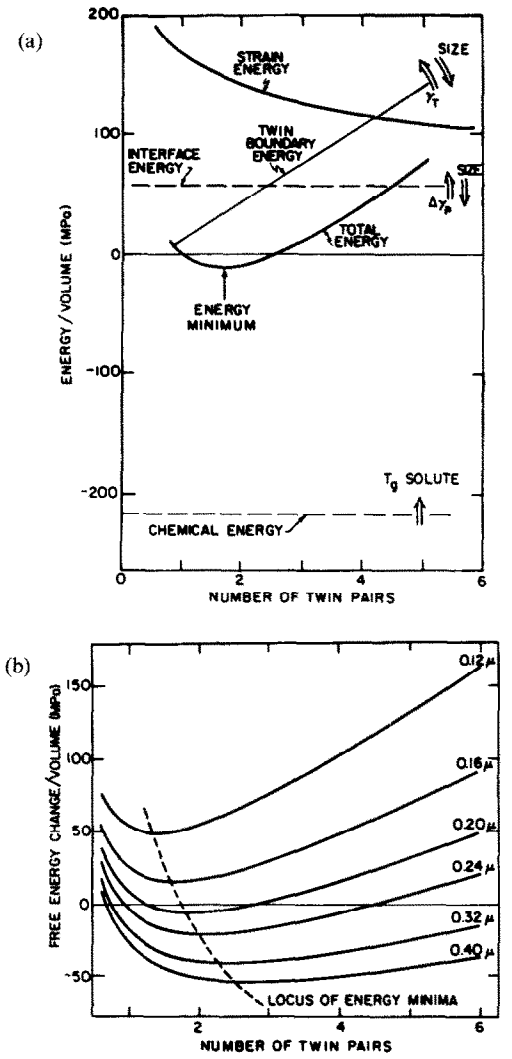

Fig. 8. (a) Variation in the energy per particle with the number of twins in an oblate spheroidal precipitate in MgO/PSZ predicted using a finite element analysis, (b) the particle size dependence of the optimum number of twins based on minimization of the total energy of the system.

Under an applied shear stress, τ, parallel to the twins, ΔG is minimized by the presence of a net shear strain. This optimum net shear is†

$$\varepsilon^{ns} \simeq \left(\frac{\eta+1}{\eta-1}\right)\frac{\tau}{\mu} \qquad (4.10)$$

†This condition pertains for a fully transformed particle. At partial transformation, the optimum net transformation strain exceeds the applied strain resulting in a net particle stress (e.g. $\tau^p = -\Delta G_0/\varepsilon_s$ from equation 5.1 with $\zeta = \Delta = 0$).

‡Numerous arguments based final energies and involving surface energy stabilization of the tetragonal phase, high twin boundary energies, or requisite concurrent cracking, have been invoked to explain the size dependencies. Such arguments are insufficient as they do not consider actual transformation paths and cannot account for the order of magnitude variations in "critical size" with concentration or history.

which can be appreciable when $\tau/\varepsilon_s\mu$ is significant. When the number of twins is large, exact cancellation of the applied strain occurs leading to elimination of the long range shear stress in the particle. Minimization of the total free energy suggests that the number of twins in the final product should satisfy

$$\eta \simeq \left\{\frac{4\mu\varepsilon_s^2 h}{\gamma_t}\left[1-\left(\frac{\varepsilon^{ns}}{\varepsilon_s}\right)^2\right]\right\}^{1/2} - 1. \qquad (4.11)$$

Thus, when $\tau/\varepsilon_s\mu$ is appreciable, the optimum number of twins is reduced. Experimental observations, primarily after thermally induced transformations, suggest that fewer twins are typically present than predicted for the stress free case, indicating that twin nucleation is a limiting factor.

4.2. The nucleation

The martensite nucleation issue is not well understood in ZrO_2 systems. There is no appreciation either of the relative applicability of classical and nonclassical nucleation concepts or of the specific embryos that initiate the transformation. The widespread experience that small particle or grain sizes expedite retention of the tetragonal phase (both in dispersions and in fully tetragonal polycrystals) suggests that heterogeneous nucleation is dominant, at least for thermally induced transformations.‡ However, extensive transmission electron microscope studies have not revealed the presence of dislocations either in the parent phase or in the matrix [2, 7, 13, 22, 28] (Fig. 2). Consequently, the various dislocation based nucleation notions [41, 42] do not appear to pertain, at least for fine particle sizes. The most plausible *deterministic* concepts regard various residual strain sites as embryos, by virtue of the relatively large, interaction energy ($\sigma_{ij}\varepsilon_{ij}^{T}$) associated with the residual field. Specifically, sites where $\sigma_{ij}\varepsilon_{ij}^{T}$ exceeds a critical value over a sufficient volume can be regarded as martensite embryos [38] (which may require thermal activation).

Appropriately large residual stresses may exist at facet corners, (Fig. 9) due to thermal expansion anisotropy or mismatch between phases. Corners typically result in logarithmically singular residual fields of the form [43, 44]

$$\sigma_{ij} \sim \Delta\alpha\Delta T\langle E\rangle \ln(l/r) \qquad (4.12)$$

where $\Delta\alpha$ is the thermal expansion mismatch, l is the facet length and r is the distance from the corner. In particular, thermal mismatch induced singularities in the residual *shear* strain exist at most corners [45] which tend to accommodate the shear strain of the transformation. This concept has the attractive feature that a size scale, l, enters the nucleation process in a natural manner and may provide a basis for the generally observed transformation size dependence. Furthermore, it could account for the observation that angular ZrO_2 particles, e.g. at grain junctions, are more susceptible to transformation than are spheroidal particles [20]. However, validation of this

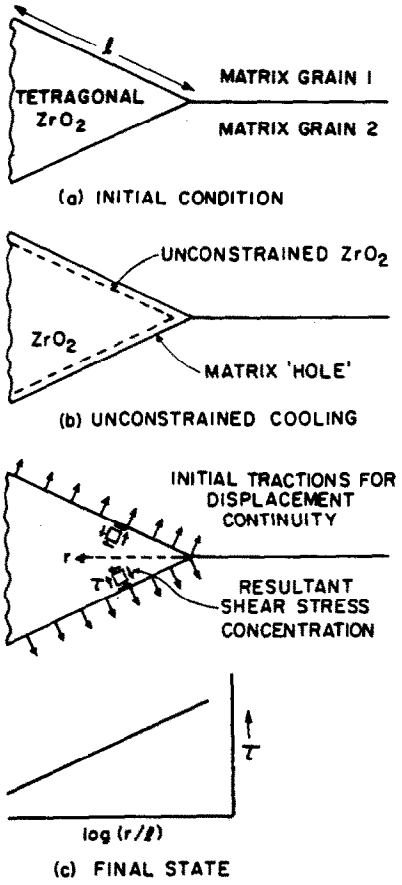

Fig. 9. A schematic illustrating the residual stress distribution near facet corners due to thermal expansion mismatch.

deterministic concept awaits detailed calculation of the energy changes associated with classical and non-classical nuclei emanating from corners.

Statistical models have also been used to describe nucleation [27, 42]. Such models are phenomenological, but constitute a convenient means of expressing trends in experimental results. Statistical models commence with the premise that the parent phase contains a distribution of nuclei, of unknown origin. The nuclei exhibit varying potency, determined by the stress (applied plus residual) and temperature. This concept can be expressed in terms of a frequency distribution, $g(\rho)\mathrm{d}\rho$, representing the number of nuclei in unit volume of parent phase with a potency between ρ and $\rho + \mathrm{d}\rho$. For present purposes, high potency refers to a low value of the driving force $(\Delta G_0 + \sigma_{ij}\varepsilon_{ij}^{\mathrm{T}})$ required to initiate transformation.

This basic frequency distribution can be used in various ways to determine the transformation characteristics of regions of parent phase contained in an inert matrix. In all instances, information regarding the number density of embryos is implicit in the statistical development. Initially, it is convenient to define a volume element ΔV of parent phase which, on average, contains a single embryo. Then, the transformation probability of independent elements of that size is directly related to the cumulative distribution of site potencies, via the Poisson postulate [46]

$$\delta\phi = \Delta V \int_{\rho^*}^{\infty} g(\rho)\mathrm{d}\rho \tag{4.13}$$

where ρ^* is the potence level at which embryos are nucleated by the imposed supercooling and stress and $\delta\phi$ is the transformation probability. The choice of ΔV, compared with the particle volume, V_p, thus constitutes the first essential decision.

When each particle contains a *large number* of embryos such that $V \ll V_p$, the presumption that activation of a single embryo transforms the entire particle (as evidence suggests for small particles) allows weakest link statistics to be used to assess the particle transformation probability [46, 47]. Specifically, the survival probability of the particle becomes the product of the survival probability of all elements ΔV within the particle, such that for $\delta\phi \ll 1$

$$\begin{aligned} 1 - \Phi &= \Pi(1 - \delta\phi) \\ &= \exp\left[-V_p \int_{\rho^*}^{\infty} g(\rho)\mathrm{d} \right] \end{aligned} \tag{4.14}$$

where Φ is the transformation probability of the particle. Furthermore, since transformation, in this instance, relates to the extreme of the nucleus potency distribution, a power law relation for $g(\rho)$ is likely to apply [48], such that

$$\int_{\rho^*}^{\infty} g(\rho)\mathrm{d}\rho = (\rho_0/\rho^*)^k \tag{4.15}$$

where ρ^* is a scale parameter and k is a shape parameter. The probability of transformation thus becomes

$$\Phi = 1 - \exp[-V_p(\rho_0/\rho^*)^k]. \tag{4.16}$$

Distinction must now be made between interacting and non-interacting particles. When the particle spacing is relatively large, such that the particles are *noninteracting*, Φ dictates the fraction f of particles that transform in accord with conventional order statistics [48]; thus

$$f = \Phi(1 + 1/N) \tag{4.17}$$

where N is the total number of particles in the body subject to the specified supercooling and stress. Consequently, the transformed fraction depends on the *particle volume*

$$f = (1 + 1/N)\{1 - \exp[-V_p(\rho_0/\rho^*)^k]\}. \tag{4.18}$$

However, modified expressions prevail in the presence of a wide particle size distribution. Then, each size class is described by Φ, and when N is large, the volume fraction transformed is

$$f = \frac{\int_0^{\infty} V\Phi h(V)\mathrm{d}V}{\int_0^{\infty} Vh(V)\mathrm{d}V} \tag{4.19}$$

where $h(V)$ is the size distribution function.

The magnitude of the effect is illustrated for the extreme case

$$\int_0^{V_p} h(V)\mathrm{d}V = 1 - \exp[-V/V_0],$$

which gives a transformed fraction

$$f = 1 - [1 + V_0(\rho_0/\rho^*)^k]^{-2}. \qquad (4.20)$$

Comparison with equation (4.18) reveals that the wide size distribution causes f to double at low driving force and results in a more persistent fraction of untransformed material at low ρ^*.

When the transformation is interface nucleated, V_p must be replaced by the *surface area* of the particle, A_p, and equation (4.20) suitably modified.

The trends suggested by equation (4.18) conform with the particle size dependence of the transformation probabilities measured both for a ZTA material with an intragranular dispersion of ZrO_2 [20] [Fig. 10(a)] and for Fe particles in Ni [42]. Conformance is achieved by assuming that the interface area controls nucleation and that the critical potency, ρ^*, varies inversely with undercooling, ΔT. However, it is noted that the transformation probabilities in the ZTA are appreciably reduced by extended annealing [20] [Fig. 10(b)]; a behavior that implies an important influence of unidentified heterogeneities or of changes in particle shape.

Interactions between particles in a colony modifies the preceding results. Specifically, for the situation in which transformation of a single particle activates an

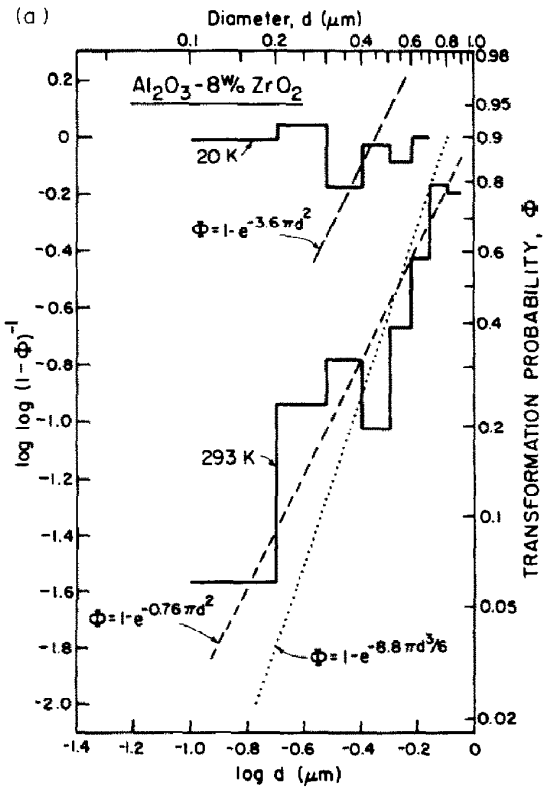

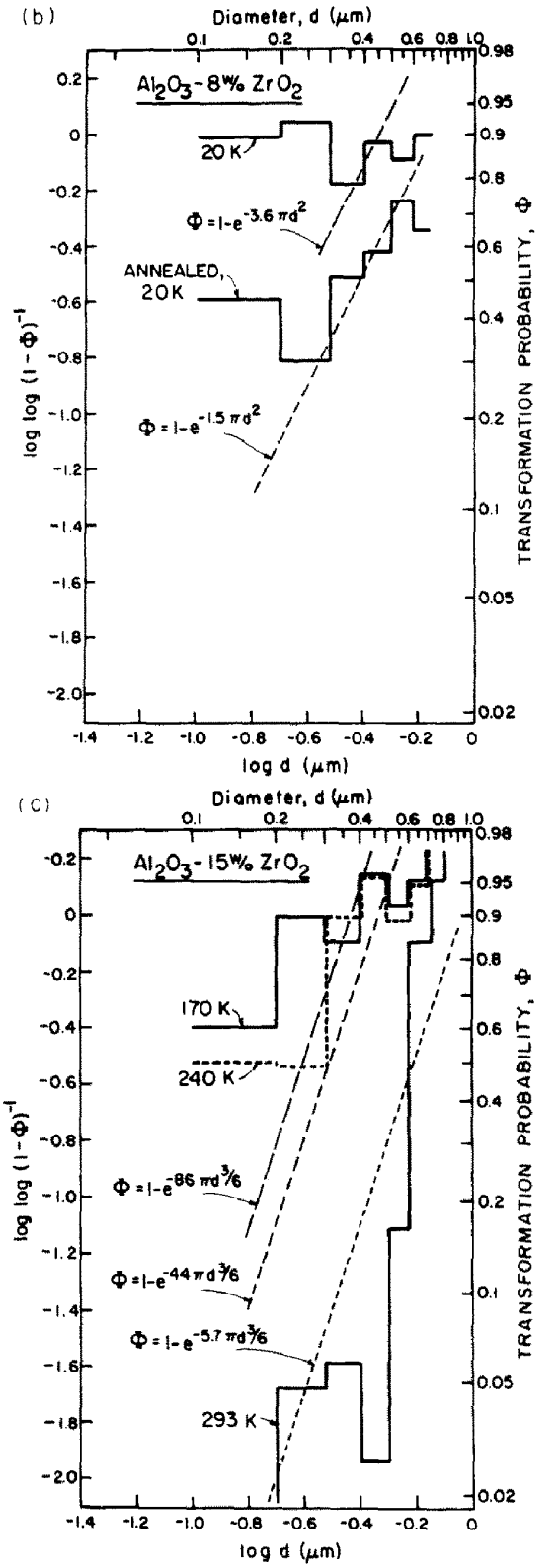

Fig. 10. Variation in the fraction of transformed particles, with particle size showing the utility of the exponential function for data fitting; (a) intragranular particles in dilute dispersion, (b) intergranular particles in dilute dispersion, which exhibit effects of prior annealing on the transformation probability, (c) intergranular particles in moderate concentration which exhibit a sharper size dependence (data from Ref. [20]).

entire colony by an autocatalytic process, V_p is replaced by the *colony volume*, V_t. The size of individual particles within the colony is of no significance if volume statistics are appropriate. Alternatively, if A_p controls the individual transformation probabilities, then V_p is replaced by $V_t(A_p/V_p)$, whereupon fine particles facilitate transformation (seemingly contrary to experience). Interaction effects are indicated by numerous cases wherein the transformation probability increases with increase in ZrO_2 concentration [27]. Such effects may also be partially responsible for the comparatively sharp transformation size dependence found in ZTA with intermediate (15%) ZrO_2 concentrations [Fig. 10(c)] [20].

Comparable statistical developments are more complex when the number density of nuclei is small. For example, when the number of nuclei per particle is minimal, the dependence of f on particle volume is less than anticipated by equation (4.14); an effect which may account for the weak size dependence in Fig. 10(b). In fact, the absence of obvious nucleation sites in ZrO_2 indicates that small density statistics (e.g. pertinent to particle corners) require development. Such statistics should be effectively coupled with deterministic analysis of corner effects.

The behavior exhibited by equations (4.7) and (4.18) or (4.19) provides a preliminary basis for development of constitutive relations. In a relatively homogeneous applied, or residual, stress field, achieving a critical free energy of embryos low enough to induce nucleation corresponds to achieving a critical interaction energy, $\sigma_{ij}\varepsilon_{ij}^{T}$. The most effective stress coupling for driving the transformation, at least for untwinned nuclei, derives from the shear strains (because of the large lattice shears in ZrO_2). Thus, embryos oriented to allow coupling with deviatoric stresses, exhibit nucleation stresses much lower than those for which only the mean stress couples with the dilation. This characteristic is illustrated in Fig. 27 in terms of zone boundaries around a loaded crack, that are based on critical values of $\sigma_{ij}\varepsilon_{ij}^{T}$. The differences in the boundaries arise from variations in the type of stress coupling owing to differences in embryo orientations or in uniformity of the dilation.† In particular, where shear coupling occurs, larger zones result. In ZrO_2, three orientation relations between the monoclinic and tetragonal have been reported, suggesting that appreciable flexibility exists for effective deviatoric stress coupling.

4.3. Growth barriers

After nucleation, the driving force for growth

$$F = -(1/A)\mathrm{d}G/\mathrm{d}n \tag{4.21}$$

follows from equation (4.1), where A is the area swept by the interface and n, the normal unit vector. It may be anisotropic owing to shape dependent elastic energies. In principle, martensite growth involves an interfacial resistance, perhaps analogous to the Peierl's barrier, or other interactions resisting dislocation motion. This could be strongly temperature and velocity dependent if thermally activated processes are important, as indicated by the plastic deformation of ZrO_2, especially below 500°C. The growth resistance may also be substantial for overdriven transformations, with interfacial velocities approaching the elastic wave speed.

†The required $\sigma_{ij}\varepsilon_{ij}^{T}$ changes modestly with the specific orientation and lattice strains which affect the embryo shape and surface energy [27].

5. DEFORMATION CHARACTERISTICS

5.1. Stress–strain-kinetic relations

Trends in the stress–strain characteristics of a solid containing a transformable phase can be described, in general terms, from the preceding thermodynamic considerations [27, 39]. Such characteristics are subsequently used to evaluate the toughness, based on curves of the type depicted in Fig. 20. This behavior may be understood by examining various fundamental features of the stress–strain curve. The simplest condition to envision is a transformation occurring in thermodynamic equilibrium ($F = \delta G = 0$), without a nucleation or other kinetic barrier. Then, for a single twin, the particles gradually transform under increasing stress. Initial spreading of a thin plate is favorable when $\sigma_{ij}\varepsilon_{ij}^{T} = -\Delta G_0 + A_0$. Below this stress, linear elastic behavior obtains. Subsequent thickening, when the transformed region is small ($a \gg h$) occurs at [39, 49] [from equations (4.4) and (4.21)]

$$\sigma_{ij}\varepsilon_{ij}^{\tau} = -\Delta G_0 + A_0 + 2A_1(h/a) + 2\gamma/a \tag{5.1}$$

and produces strain, in addition to the elastic strain, of

$$\varepsilon_{ij} = f\varepsilon_{ij}^{T} \tag{5.2}$$

where f, the current volume fraction transformed, is $\sim(h/a)f_{\max}$. However, more complex stress dependencies obtain as the transformed region further thickens. The specific shape of the stress–strain curve depends on particle geometry but usually, the slope $\mathrm{d}\sigma/\mathrm{d}\varepsilon$ decreases as the transformation nears completion. Once transformation is complete, linear elastic behavior is reestablished. This occurs at a stress σ_{ij}^{*} given by

$$\sigma_{ij}^{*}\varepsilon_{ij}^{T} \simeq -\Delta G_0 + A_2 + A_3 \tag{5.3}$$

where

$$A_2 = \frac{2(1+\nu)}{9(1-\nu)}\mu\Delta^2 + \frac{8}{45}\frac{(3-\nu)}{(1-\nu)}\mu\xi^2 + \frac{4}{9}\frac{(1+\nu)}{(1-\nu)}\mu\xi\Delta$$

and

$$A_3 = \frac{2(7-5\nu)}{15(1-\nu)}\mu\varepsilon_s^2. \tag{5.4}$$

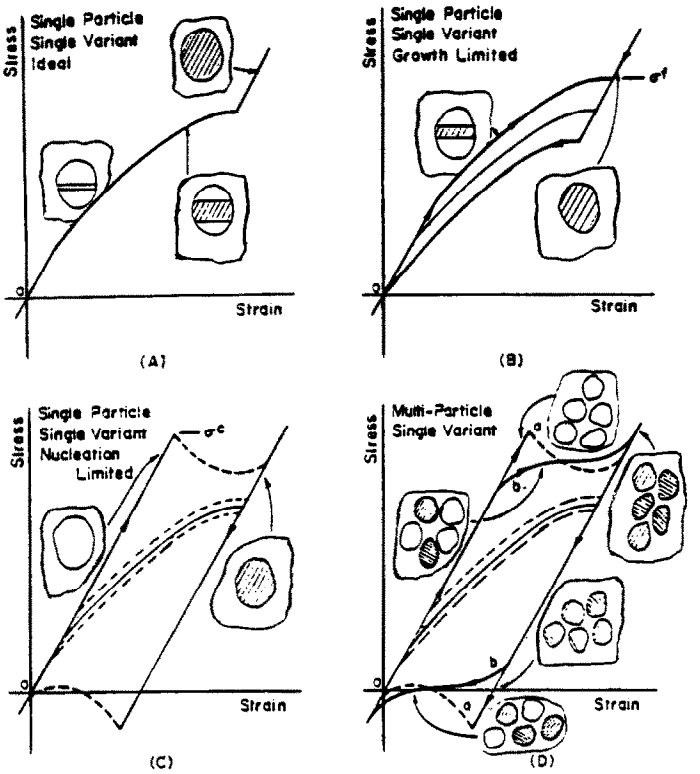

Fig. 11. Schematic illustration of the stress–strain behavior expected for various controlling transformation kinetics in the absence of twinning (courtesy T. W. Coyle).

This stress–strain curve must, by definition, be fully reversible, i.e. the chemical and elastic energy changes compensate for each increment of transformation.

The preceding behavior is modified if the motion of the martensite interface exhibits frictional resistance, requiring $F = \hat{F}$. Then, hysterisis is imposed (Fig. 11). Typically, a nucleation barrier also exists, which may be substantial. The effect of such a barrier is to increase the critical transformation stress above the equilibrium value. Furthermore, once nucleation conditions have been satisfied, extensive transformation proceeds, under diminishing load, until either quasistatic equilibrium (i.e. with $F = \hat{F}$) is reestablished or complete particle transformation has occurred (Fig. 11).

The incidence of twinning influences certain details of the stress–strain behavior. In particular, the opposing shear strains in neighboring twins suggests that alternate twins may form with decreasing load. A serrated stress–strain curve is thus expected (Fig. 12). Consequently, the net slope, $d\sigma/d\varepsilon$ of the elastic equilibrium curve is much smaller than that for

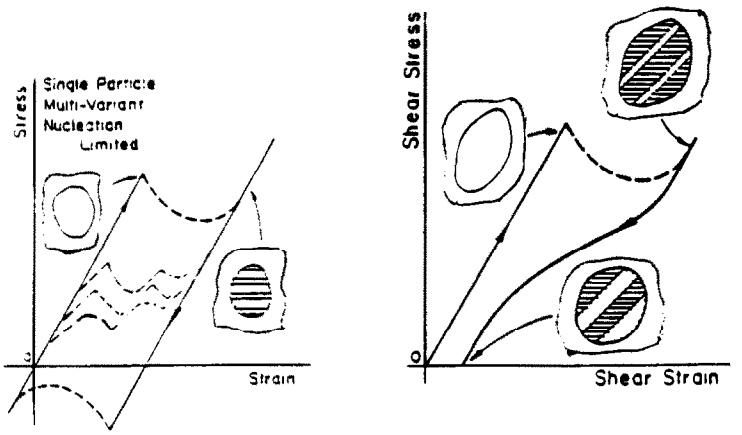

Fig. 12. Schematic indication of the effect of twinning on the stress–strain curves (courtesy T. W. Coyle).

untwinned particles; it may even be negative if all deviatoric strains are compensated. The stress to complete transformation is [27, 39]

$$\sigma_{ij}^{*}\varepsilon_{ij}^{nT} \simeq -\Delta G_0 + A_2 + U_s + \hat{F} \qquad (5.5)$$

where U_s is taken from equation (4.9) or modified for the appropriate twin geometry. This is a lower bound, because additional stress is required to nucleate and extend twins. Moreover, only the net strains, ε_{ij}^{nT}, contribute to the macroscopic strain, equation (5.2).

After nucleation involving a sufficiently large barrier, the stress is controlled by the compliance of the surrounding material, which dictates the rate at which unloading can occur. Then, the stress at completion of transformation is

$$\sigma_{ij}^{*} = \sigma_{ij}^{c} - \sigma_{ij}^{r} \qquad (5.6)$$

where σ_{ij}^{c} is the nucleation stress and σ_{ij}^{r} is the residual stress which would be imposed on the composite element by emplacing it in the surrounding, untransformed material with no applied stress. Regardless of whether the stress is controlled by $F = \hat{F}$ or by equation (5.6), the area under the stress–strain curve between the actual stress and the ideal (equilibrium) stress represents energy which is immediately dissipated as heat either by static, interfacial drag processes or by dynamic, phonon processes.

Several factors may control the actual internal structure and net transformation strains which develop, including the transformation strains and surface energies associated with the specific crystallographic orientations of the martensite. In addition, the macroscopic transformation strains may vary during transformation. Initially, (i.e. while the transformed region is still thin) the strain energies are lower if the transformation strains approximate an invariant plane strain (IPS) [38]. However, in the late stages of transformation, pure dilation may be energetically preferable [39]. Consequently, the structures represent a kinetically limited, history dependent compromise, influenced by the level of applied stress.

Of the myriad of possible internal structures, three idealizations (based on individual variants that each have an IPS strain) illustrate important characteristics which influence toughening behavior. (1) In a *tensile field* with the tensile axis normal to the twin planes, uniformly spaced twins that cancel the out-of-plane shears would be energetically preferable. The volume change would appear as a uniaxial extension, aligned with the tensile stress. Importantly, the long range transformation strain, $\varepsilon_{11}^{T} = \xi$ would be independent of the maximum stress achieved and would be unchanged upon unloading.† (2) Alternatively, if the twins were aligned parallel to a significant *shear stress*, an additional net shear strain developed by unevenly spaced twins would be greater for a higher shear stress [equation (4.10)]. The optimum net shear is similar to or exceeds the applied elastic strains. Thus, the final transformation strain would depend upon the stress level throughout transformation. An additional distinction is that upon unloading, the shear strain could be reduced simply by migration of the twin boundaries, [Fig. 12(b)]. (3) Finally, at *low applied stresses* or in a *hydrostatic field*, pure dilation could be approximated by means of more complex arrangements of nonparallel variants. Obviously, if the transformation strains for individual variants do not satisfy an IPS condition, the details are altered, but the important features remain. Furthermore, the probability of realizing any of these configurations depends partially on the orientation of the tetragonal particle in the stress field and the influence of applied stress on the variants which nucleate.

The stresses characterizing the stress–strain curves include components needed to surmount the several kinetic barriers, plus components necessary to overcome the elastic strain energy. In all cases, stresses required to surmount the latter are an essential prerequisite to forward transformation. Furthermore, it should be recognized that the elastic energies would cause transformation reversal in the absence of reverse kinetic barriers. The elastic driving force for reverse transformation is appreciably lowered only when a significant fraction of the total sample is transformed and the deviatoric transformation strains are substantially self-compensated [27, 39]. To assess the relative importance of these factors, particularly for behavior around crack tips, it is expedient to distinguish small and large particles.

For *small* particles, having a paucity of nucleation sites, the transformation may be completely nucleation limited. As such, nucleation would occur at a critical stress, σ_c, and complete transformation would ensue immediately. Furthermore, when the nuclei potency is similar for all particles, the stress–strain curves would be mechanically unstable, e.g. $d\sigma/d\varepsilon < 0$ and the actual curve may be controlled by the compliance of the material surrounding the transformation zone. The stress–strain curves for this situation can be characterized in terms of σ_c and the net transformation strains, unless twin rearrangement or transformation reversal occurs upon unloading. In contrast, a wide distribution of nuclei potencies would lead to stable stress–strain behavior, $d\sigma/d\varepsilon > 0$, which could be characterized using statistical expressions, equation (4.19).

For *larger* particles, several important differences may arise. When the initial nucleation stresses are low, complete transformation may not occur without a further increase in stress. The stress to complete transformation would then depend upon requirements either for further thickening of the martensite plates or for nucleation of successive twins. In addition, the variation in the crack tip stresses through-

†Alternatively, the classical model of martensite forming with an IPS interface and oblique, trailing twins would give a fixed elongation, normal to the interface, plus a fixed parallel shear.

out the particle may not be trivial. Then, even if σ_c is large, the transformation may be initiated by nucleation near the crack tip and the extent of the zone would be determined by obstacles to plates. Furthermore, the transformed population within the zone may depend upon the stresses required to complete transformation. Somewhat analogous behavior may obtain for small particles at high concentrations owing to interparticle interactions and autocatalytic nucleation.

5.2. Constitutive laws

The preceding general description in terms of the energy changes and kinetic requirements associated with transformation can be used to construct idealized, but quantitative constitutive laws [10, 50] which, in turn, allow prediction of transformation toughening. Constitutive laws, thus derived, expressly relate the components of the stress and strain tensor in the transforming solid. These are most conveniently expressed in terms of the mean stress, $\bar{\sigma}$, the deviatoric stresses, s_{ij}, and their variation during transformation. Such relations are, in fact, the equivalent of the more familiar constitutive laws used to describe plastic deformation and crack tip fields in elastic/plastic solids.

A viable constitutive law must account for the effect of particle size and shape upon the incidence of transformation by allowing only a certain fraction, f, of the transformable solid to actually transform at a given stress σ_{ij}. Then, f and the average σ_{ij} are related by [10]

$$\sigma_{ij} = f\sigma_{ij}^{p} + (1-f)\sigma_{ij}^{m} \tag{5.7}$$

where the superscripts p and m refer to the particles and matrix, respectively. The stresses in the particle can be deduced directly from the Eshelby solutions [37], given the particle shape, the transformation strains etc. Hence, the stresses in the system can be uniquely described in terms of the matrix stresses, σ_{ij}^{m}. Consequently, a generalised *critical transformation condition* can be written as [50]

$$\Omega(\sigma_{ij}^{m}) = H(f) \tag{5.8}$$

where the functions Ω and H are to be determined for each particle condition of interest. Furthermore, $H(f)$ has been established as a monotonically increasing function of f, dependent on the geometry of the transforming region. Hence, a *criterion for continued transformation* may be expressed as [50]

$$\mathrm{d}\Omega(\sigma_{ij}^{m}) > 0. \tag{5.9}$$

Finally, since each increment in f introduces a corresponding increment of inelastic strain, ε_{ij}, the *flow rule* has the form

$$\mathrm{d}\varepsilon_{ij} = g_{ij}(\boldsymbol{\sigma}^{m})\mathrm{d}f. \tag{5.10}$$

For any transformable system, complete specification of the constitutive laws requires that Ω and g_{ij} be determined from independent knowledge of the transformation characteristics. The results derived in the preceding section can be used for this purpose. Specifically, by expressing the Gibbs free energy change for transformation as

$$\delta G = \delta G^{+} - V\varepsilon_{ij}^{T}(\sigma_{ij}^{m} + \sigma_{ij}^{p}/2) \tag{5.11}$$

where δG^{+} refers to all "nonmechanical" terms in equation (4.1), and requiring that for transformation, $\delta(G - G_c) < 0$ the critical transformation criterion has been approximated as

$$(\sigma_{ij}^{m} + \sigma_{ij}^{p}/2)\,\varepsilon_{ij}^{T} = (\Delta G_c - \Delta G_0) \tag{5.12}$$

where ΔG_c is the excess free energy per unit transformed volume associated with nucleation or growth. The left hand side of equation (5.11) can be related to the requisite function, $\Omega(\sigma_{ij}^{m})$. Further progress requires that the particle shape be specified and that some statement be made regarding the shear stresses that develop after transformation. Several results have been derived in the literature. Most of these derivations have assumed that linear elastic behavior obtains both prior to a critical transformation condition, $\sigma_{ij}^{c}\varepsilon_{ij}^{T}$, and after transformation is complete. Thus, the resultant stress–strain curves are often comprised entirely of linear segments.

For the purely dilatational transformation, the constitutive law for the composite material is independent of the shape of the transforming region and (for plain strain) has the form [10]

$$\sigma_{\alpha\beta} = 2\mu(\varepsilon_{\alpha\beta} - \varepsilon_{\mu\mu}\delta_{\alpha\beta}/3) + B(\varepsilon_{\mu\mu} - f\varepsilon_{ii}^{T})\delta_{\alpha\beta} \tag{5.13}$$

$$\sigma_{33} = -2\mu\varepsilon_{\mu\mu}/3 + B(\varepsilon_{\mu\mu} - f\varepsilon_{ii}^{T})$$

$$\bar{\sigma} = (1+\nu)\sigma_{\mu\mu}/3 + Ef\varepsilon_{ii}^{T}/9$$

with

$$\varepsilon_{\alpha\beta} = (\sigma_{\alpha\beta} - \nu\sigma_{\mu\mu}\delta_{\alpha\beta})/2\mu + (1+\nu)f\varepsilon_{ii}^{T}\delta_{\alpha\beta}/3. \tag{5.14}$$

When the shear component of the transformation is also considered, expressions pertinent to spherical and oblate spheroidal particles have been derived for the case where the shear stress in the particle after transformation is assumed to be zero, viz

$$s_{ij}^{p} = 0 \tag{5.15}$$

with, $s_{ij} = \sigma_{ij} - \bar{\sigma}$. This assumption is tantamount to presuming that the twins in the transforming particle are free to adjust to the applied stress in such a manner that the resultant shear stresses vanish. This assumption is a useful limiting condition, equation (4.10), although the validity is difficult to assess. With the premise specified by equation (5.15), the constitutive laws have the following forms. For spherical particles [50]

$$\Omega(\sigma_{ij}^{m}) = M[\sigma_e^{m}/P]^2 + \bar{\sigma}^{m}/P \tag{5.16}$$

where

$$P = B\varepsilon_{ij}^{T}\delta_{ij} \tag{5.17}$$

$$\sigma_e^2 = (3/2)s_{ij}s_{ij}$$

$$M = B/6(1-\beta)$$

$$\beta = 2(4\text{–}5\nu)/15(1-\nu)$$

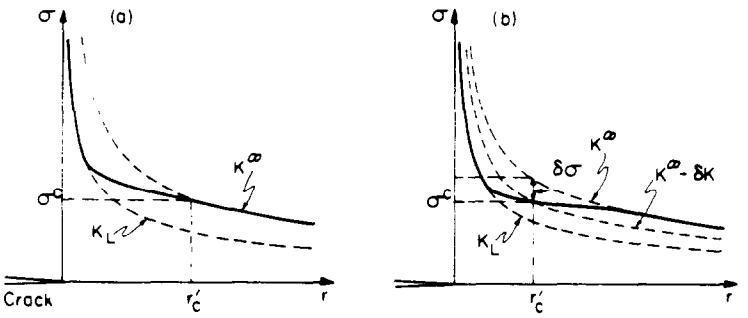

Fig. 13. Crack tip stress fields in the presence of a dilational transformation zone: (a) for a supercritical transformation, and (b) for a subcritical transformation with $\bar{B} > 0$.

with B the bulk modulus and μ the shear modulus. The corresponding inelastic strains in the flow rule are

$$d\varepsilon_{ij} = \varepsilon_{ij}^{T} df \tag{5.18}$$

and

$$de_{ij} = e_{ij}^{T} df \tag{5.19}$$

where ε_{ij}^{T} is assumed to be constant and the relaxed deviatoric stess condition leads to

$$e_{ij}^{T} = s_{ij}^{m}/2\mu(1-\beta) \tag{5.20}$$

with

$$e_{ij} = \varepsilon_{ij} - \varepsilon_{pp}\delta_{ij}/3. \tag{5.21}$$

The nonlinear term in Ω results from the assumption expressed in equation (5.20). For thin oblate spheroids, corresponding approximate solutions† are [50]

$$\Omega(\sigma_{ij}^{m}) = S_{33}^{m} A_{22}/2A_{11} + \bar{\sigma}^{m} \tag{5.22}$$

$$d\varepsilon_{ij} = \varepsilon_{ij}^{T} df \tag{5.23}$$

$$de_{11} = de_{22} = -(A_{22}/3A_{11})\varepsilon_{ii}^{T} df \tag{5.24}$$

$$de_{33} = (2A_{32}/3A_{11})\varepsilon_{ii}^{T} df$$

$$de_{ij} = 0 \text{ (for } i \neq j)$$

where

$$A_{11} = 1 - \left(\frac{3\pi R}{8}\right)\left(\frac{1+4\nu}{1+\nu}\right) \tag{5.25}$$

$$A_{22} = 1 - 3\pi R/4$$

with R being the aspect ratio of the spheroid.

The preceding constitutive laws, or their equivalent for other shear assumptions, provide the basis for determining crack tip fields and hence, for predicting trends in transformation toughening, as discussed in the subsequent sections.

†This expression for Ω presumes that the shape induced deviatoric stresses in particles dominate over the applied stresses; the implications are most important for small transformation zones [50].

‡The analytical expressions subsequently presented are based on the small strain limits for $f_{ij}(\theta)$.

6. TRANSFORMATION TOUGHENING

The current analyses of transformation toughening describe various aspects of the problem which, in combination, provide compelling arguments concerning trends in toughness with zone size and shape, R-curve effects, and the relative influence of the dilatational and shear components of the transformation strain. The initial basis for the analytic development entails consideration of the effects of transformation on the stress field around the crack. Thereafter, the stresses induced by various transformed areas can be used to derive expressions for the toughness, and its dependence on zone shape including the extension behind the crack tip and the frontal profile. The analogous thermodynamic calculation of the toughness is then shown to predict the same behavior as the stress-based analysis, giving substantial credence to present, fundamental understanding of the toughening process. Lastly, effects that arise when the population of transformed material varies within the zone are examined.

6.1. Crack tip stress fields

The general form of the crack tip stress field in the presence of a transformation zone, depicted in Fig. 13, is characterized by two stress intensity factors [9]. Outside the transformation zone, for small scale yielding conditions (i.e. a small transformation zone compared with crack length and specimen dimensions), the field is given by the linear elastic solution ($h < r \ll a$)

$$\sigma_{ij} = (K_{\infty}/\sqrt{2\pi r}) f_{ij}^{0}(\theta) \tag{6.1}$$

where K_{∞} is the stress intensity determined by the applied loads and r is the distance from the crack tip. Close to the tip, the transformation strain is saturated and hence, the material is again linear and can, consequently, be characterized by another stress intensity factor, K_{tip} [9], such that

$$\sigma_{ij} = (K_{tip}/\sqrt{2\pi r}) f_{ij}^{i}(\theta). \tag{6.2}$$

The coefficients, $f_{ij}(\theta)$, which depend on polar angle, approach those for elastic materials when the $f\varepsilon_{ij}^{T}E/\sigma_{c}$ are small [10, 50].‡

The transformation may thus be characterized by a stress intensity change ΔK, defined as

$$\Delta K = K_{tip} - K_{\infty}. \quad (6.3)$$

When $K_{tip} < K_{\infty}$, ΔK is negative and the transformation zone shields the tip from the applied loads.

The fracture behavior is governed by the values of K_{tip} and K_{∞} at the fracture criticality. Knowledge of the stress in the intervening regions ($y \sim h/2$) is not required for analysis of the toughening [10]. Specifically, the near tip field provides the crack extension criterion

$$K_{tip} = K_0 \quad (6.4)$$

where K_0 is the fracture *resistance* of the material in the transformation zone immediately ahead of the crack tip; whereupon, the *observed toughness* is

$$K_c = K_0 + \Delta K_c \quad (6.5)$$

where ΔK_c is the quantity $-\Delta K$, evaluated at the fracture criticality.

The change in stress intensity caused by the zone can be expressed in terms of an integral over the zone as [9, 50]

$$\Delta K = \int\int dK_{tip} \quad (6.6)$$

where dK_{tip} is the stress intensity induced by two small cylindrical zones, of area dA, located at $(r, \pm\theta)$ with respect to the tip, such that [51]

$$dK_{tip} = EM\ (\chi, \theta)\, dA/\sqrt{8\pi}\, r^{3/2}(1 - \nu^2) \quad (6.7)$$

with M determined by the stress free strains χ

$$M = \chi_{\alpha\alpha} \cos 3\theta/2 + 3\chi_{12} \cos 5\theta/2 \sin\theta + [3(\chi_{22} - \chi_{11})/2] \sin\theta \sin 5\theta/2 \quad (6.8)$$

such that, for plane strain

$$\chi_{11} = (1 + \nu) f\varepsilon^T_{ii}/3 - \nu e_{\mu\mu} + e_{11}$$
$$\chi_{22} = (1 + \nu) f\varepsilon^T_{ii}/3 - \nu e_{\mu\mu} + e_{22}$$
$$\chi_{12} = e_{12}. \quad (6.9)$$

Some examples of ΔK calculations are presented in the subsequent sections.

6.2. Stress intensity factors

The magnitude of ΔK clearly depends on the shape of the zone and on the components of the transformation strain. Initially, it is pertinent to consider a crack in an untransformed parent, such that a *frontal zone* develops as the load is imposed. Subsequently, a *steady-state zone* of uniform width over the crack surfaces (Fig. 14), is examined. The ΔK levels are different for these two zone configurations, resulting in potential R-curve effects [9].

†This result obtains for any partially transformed zone for which contours of constant f follow constant $\bar{\sigma}$ contours.

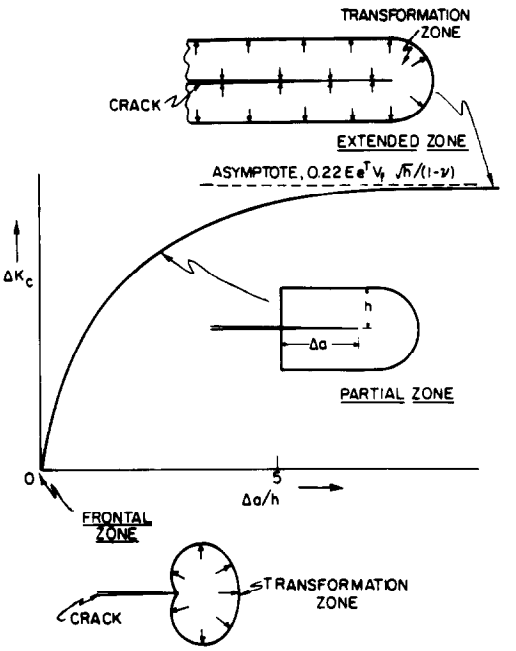

Fig. 14. Transformation zones illustrating the dimensions used in describing the transformation toughening process: a frontal zone and a steady-state zone for a dilatational driven transformation. R-curve for zones with intermediate profiles is also shown (Ref. [34]).

(*i*) *Frontal zone.* When the long range strain field of the transformed particles is purely dilatational (i.e. an extensively twinned particle with uniform twins and thereby, no long range shear strain), the mean stress may dictate the shape of the transformation zone, which then has the shape depicted in Fig. 14. For this condition, the $\int\int dK_{tip}$ calculation indicates that† $\Delta K = 0$ [9, 53]. This result is shown in Section 6.3 to be a natural consequence of the path independence of the J integral for the frontal zone.

However, zone shape effects on ΔK may be important. Such effects arise because transformed dilatant regions ahead of the crack provide deleterious, *positive* ΔK contributions ($K_{tip} > K_{\infty}$) whereas those regions at $\theta > \pi/3$ provide negative contributions (Fig. 16) [34]. Thus, if the zone profile is determined by the local shear stresses that cause nucleation of the first variant within each particle, the zone shape (Fig. 27) is flattened relative to that determined by coupling with the dilatation. Consequently, $\Delta K < 0$ and toughening obtains. Similar effects would arise for zone profiles not determined explicitly by the crack tip field, but by localized stress concentrations. Behavior of this type may obtain when transformation occurs by an autocatalytic process, notably in the form of shear bands emanating from the crack tip (Fig. 15). Again toughening would arise if most of the bands were located at $\theta > \pi/3$.

Negative values of ΔK ($K_{tip} < K_{\infty}$) have been reported when net shear strains are considered to be relaxed [50]. However, for a typical concentration of particles, the effect is small, viz. for $f = 0.3$,

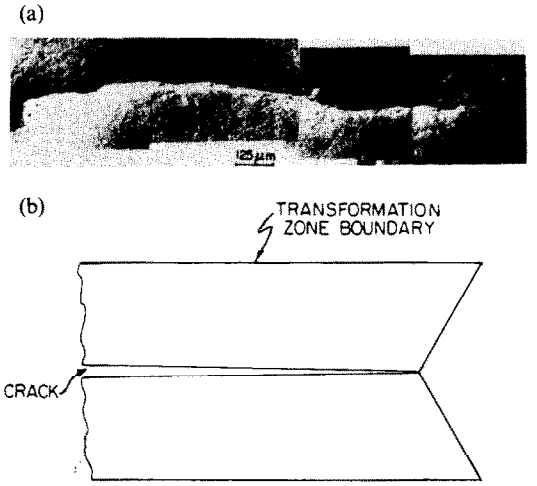

Fig. 15. Shear band transformation processes around a crack (a) optical micrograph (courtesy M. V. Swain), (b) schematic of a steady-state zone defined by a shear band mode of deformation.

$\Delta K/K \approx -0.07$ at low σ_c. It is presumed that the small effect arises because the deformation law does not yield a fully path independent J.

(ii) Steady state zone. The calculation of ΔK for the steady state configuration is, again, most straightforward for the purely dilatational transformation. For this case, when the transformation does not reverse in the wake, and when all particles within h are transformed, referred to as *supercritical* transformation, the zone width is [9, 10]

$$h = \frac{\sqrt{3}(1+\nu)^2}{12\pi}\left(\frac{K_\infty}{\bar{\sigma}_c}\right)^2 \qquad (6.10)$$

where $\bar{\sigma}_c$ is the critical mean stress to initiate transformation. The corresponding extent of crack shielding is [9, 10]

$$\Delta K = -0.22\, Ef\varepsilon_{ii}^{T}\sqrt{h}/(1-\nu). \qquad (6.11)$$

Combining the preceding results with equation (6.5), the supercritical toughness can be expressed in the following forms

$$\Delta K_c \equiv \Delta K_d = 0.22\, Ef\varepsilon_{ii}^{T}\sqrt{h}/(1-\nu) \qquad (6.12)$$

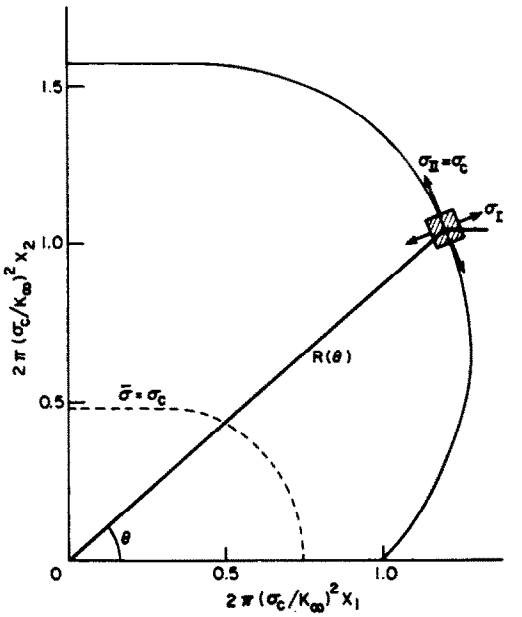

Fig. 17. The transformation zone shape for the uniaxial transformation strain condition; for comparison the dilatational zone contour is also shown (dashed) (courtesy J. C. Lambropoulos).

or

$$\Delta K_c/K_c = (\sqrt{3}/12\pi)\,(1+\nu)\,Ef\varepsilon_{ij}^{T}/\bar{\sigma}_c(1-\nu) \qquad (6.13)$$

or

$$K_c/K_0 = [1-(\sqrt{3}/12\pi)\,(1+\nu)\,Ef\varepsilon_{ii}^{T}/\bar{\sigma}_c(1-\nu)]^{-1}. \qquad (6.14)$$

Note that, if the transformation is not activated by the hydrostatic crack tip field, but occurs in shear bands, induced at $\sim\pi/3$ to the crack plane, all of the deleterious transformations in front of the crack are excluded (Fig. 15). The supercritical ΔK_c, than, increases to

$$K_c \equiv \Delta K_{sd} = 0.38\, Ef\varepsilon_{ii}^{T}\sqrt{h}/(1-\nu). \qquad (6.15)$$

Zone profile considerations are thus of prime importance in determining the magnitude of the transformation toughening.

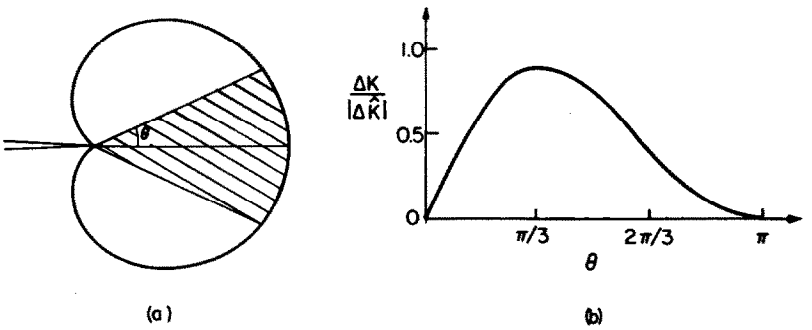

Fig. 16. Effect of particle location on the cumulative contribution to ΔK of transformed particles in a frontal zone. Particles in front of the crack increase K_{tip}; whereas particles at the side, $\theta > \pi/3$, reduce K_{tip} (Ref. [34]).

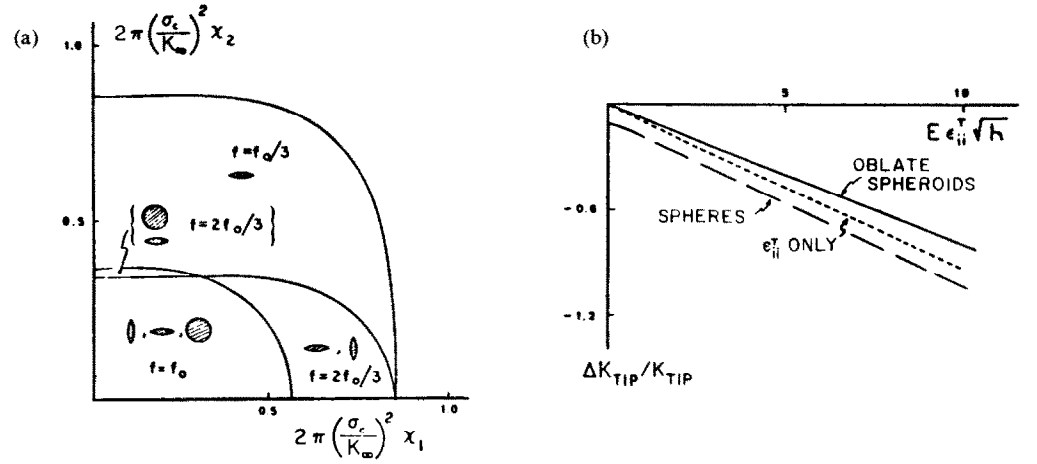

Fig. 18. Contribution to steady-state ΔK from dilation plus shear relaxation: (a) shows regions around the crack within which various combinations of the three orientations of oblate precipations for MgO/PSZ are transformed; (b) shows the toughness enhancement, ΔK_{tip} vs $E\varepsilon_{ii}^{T}\sqrt{h}$, for crack growth as induced by all three orientations of oblate precipitates, or by spherical particles ($\nu = f = 0.3$); the purely dilational result is shown for comparison (courtesy J. C. Lambropoulos).

Another relatively simple case concerns spherical particles subject to a uniaxial transformation strain $\varepsilon_{11}^{T} = \varepsilon_{ii}^{T}$ (i.e. long-range mean and shear transformation strains of equal magnitude). In particular, when the particles transform in response to the largest principal tensile stress, such that the transformation strain axis coincides with the direction of crack tip principal stress, the transformation criterion can be expressed as [50]

$$\max[\sigma_{\mathrm{I}}, \sigma_{\mathrm{II}}, \sigma_{\mathrm{III}}] = \sigma_c \tag{6.16}$$

with

$$\left.\begin{matrix}\sigma_{\mathrm{I}}\\ \sigma_{\mathrm{II}}\\ \sigma_{\mathrm{III}}\end{matrix}\right\} = \frac{K_\infty}{\sqrt{2\pi r}}\left\{\begin{matrix}1-\sin\theta/2\\ 1+\sin\theta/2\\ 2\nu.\end{matrix}\right. \tag{6.17}$$

For this situation, the zone shape is depicted in Fig. 17, and the zone width is given by [50]

$$h = (0.8/\pi)\,(K_\infty/\sigma_c)^2 \tag{6.18}$$

The change in K deduced from equation (6.6) and (6.7), provided that the transformation strain develops only at the transformation front (i.e. with no adjustment of stress by subsequent twinning within the zone) is given for the supercritical transformation by [50]

$$K_c \equiv K_u = 0.55\, Ef\varepsilon_{ii}^{T}\sqrt{h}. \tag{6.19}$$

This result reveals that special modes of transformation shear within the particles can produce substantially more toughening than the dilatation alone. In particular, this occurs when the twinning in the particle adjusts to allow the uniaxial strain to align with the maximum principal tension at *each* location along the zone front.†

Finally, the supercritical toughness has been numerically calculated under the condition that the net shear stresses within the particle are relaxed [i.e. equation (5.14)]. For oblate spheroidal particles with three orthogonal orientations, typical of MgO/PSZ, the toughening exhibits the trend depicted in Fig. 18 [50]. One orientation yields larger ΔK than does the dilatational case, while the other two afford reduced shielding. The net effect, with all three orientations present in equal proportion, is a slightly smaller $\Delta K_c/\sqrt{h}$ than for the purely dilatational transformation [50] (Fig. 18). For spherical particles, subject to the same condition, the predicted $\Delta K_c/\sqrt{h}$ slightly exceeds that for pure dilation [50]. However, it is anticipated that at large particle concentrations the toughness subject to this shear condition should approach that for uniaxial strain.

The important ΔK_c characteristics that derive from the preceding considerations are summarized in Table 1.

6.3. The strain energy release rate

The thermodynamics of crack advance can be examined by applying conventional Griffith concepts [34, 84] or by adopting energy balance integrals [10]. The latter approach permits rigorous analysis while the combination offers insights and methods needed to address more complex toughening situations.

(*i*) *The Griffith approach.* For the Griffith approach, the excess free energy of a sample relative to that of the uncracked and untransformed sample, of width l, may be expressed as

$$G = U + U_0 - W - \Delta G_0 fV + 2\gamma al + \Sigma\Delta\gamma_i A_{vi} fV \tag{6.20}$$

†The twins then exhibit different orientations or thickness at different distances from the crack plane.

Table 1. Results of steady state toughness calculations

Net strain coupling	Zone shape	Toughness	Comment
Dilation	Hydrostatic contour	$\frac{0.22Ef\varepsilon_{ii}^{T}}{(1-\nu)}\sqrt{h}$	Supercritical. No reversal
Dilation	Hydrostatic contour	$\frac{0.21Ef\varepsilon_{ii}^{T}}{(1-\nu)}\sqrt{h}$	Supercritical. Reverses with max. hysteresis
Dilation	Shear-band profile	$\frac{0.38Ef\varepsilon_{ii}^{T}}{(1-\nu)}\sqrt{h}$	Supercritical. No reversal
Uniaxial dilation	Maximum principal stress contour	$0.55Ef\varepsilon_{ii}^{T}\sqrt{h}$	Supercritical. No reversal
Dilation and relaxed shear strain	Relaxed shear front	$\sim\frac{0.22Ef\varepsilon_{ii}^{T}}{(1-\nu)}\sqrt{h}$	Supercritical. No reversal

where W is the mechanical energy in the loading device, and U the strain energy resulting from the applied load and the displacement increment caused by transformation or cracking. The residual strain energy deriving from transformation, U_0, depends upon the transformation zone volume, V, and if net shear develops, on zone shape. Similarly, the quantity $-(W-U)$ includes a component caused by transformation, $-U_I$, and another from cracking, $-U_1$. Finally, γ is the crack surface energy (assumed to be the same with either the tetragonal or monoclinic phase), and the A_{vi} are the specific areas of various internal surfaces having new or changed energy, $\Delta\gamma_i$ owing to transformation (which may include microcracks). Thus, the free energy change with increment of crack extension is

$$\frac{dG/l}{da} = -\frac{d(U_1+U_I)}{l\,da} + \frac{dU_0}{l\,da} - (\Delta G_0 - \Sigma\Delta\gamma_i A_{vi})\frac{df V}{l\,da} + 2\gamma. \quad (6.21)$$

For a perfectly reversible system, a frontal transformation zone, developed during loading, would simply advance with the crack during steady state extension. Forward and reverse transformation would occur near the leading and trailing zone boundaries, respectively. Hence since $dV/da = 0$, crack extension would occur when $dG/da = 0$ such that

$$\frac{dU_1}{l\,da} \equiv \mathcal{G} = 2\gamma. \quad (6.22)$$

Thus, a perfectly reversible transformation yields no toughening, even though it may induce nonlinear stress–strain behavior.

In real systems, additional work is required to drive both the transformation and fracture processes; whereupon, crack extension occurs at some critical value of $dG/da < 0$ (which depends upon the controlling mechanisms). The attendent dissipation, which causes hystersis, may be characterized in terms of the resultant irreversible heat flow out of the (isothermal) system, dQ_{ir}. This quantity can be determined from a total energy balance, wherein the reversible heat flow is identified from the system entropy change, as TdS. Of particular interest is the resultant association between the free energy change from incremental cracking or transformation at any particular load (L) and the irreversible heat flow

$$dQ_{ir} \equiv dQ - TdS < 0 = dG_{L,T}. \quad (6.23)$$

Thus, to allow for irreversibility, first consider crack advance in a system with no (or complete) prior transformation, then

$$\frac{dG}{l\,da} = -\frac{dQ_{ir}}{l\,da} \equiv \Gamma \quad (6.24)$$

whereupon, the condition for crack extension is

$$\mathcal{G} = 2\gamma + \Gamma \equiv \mathcal{G}_0 \quad (6.25)$$

where $\mathcal{G}_0$ is the reference toughness (which can be modified to include deflection and microcrack degradation effects, Section 9). When transformation accompanies crack advance, then

$$\frac{dG}{l\,da} = -\Gamma - \frac{dQ_{irt}}{l\,da} \quad (6.26)$$

where dQ_{irt} is the heat dissipation associated with driving the transformation forward (and possibly backward). The transformation induced toughening is thus

$$\Delta\mathcal{G}_c = \left\{\frac{dU_0}{df V} - \frac{dU_I}{df V} - \Delta G_0 + \Sigma\Delta\gamma_i A_{vi}\right\} \times \frac{df V}{l\,da} - \frac{dQ_{irt}}{l\,da}. \quad (6.27)$$

The respective role of the terms in equation (6.27) may be evaluated by considering the loading and unloading cycles of individual elements through their specific stress–strain curves (and then summing the local dissipation and stored energy over the volume). Specifically, the energy change in an element of

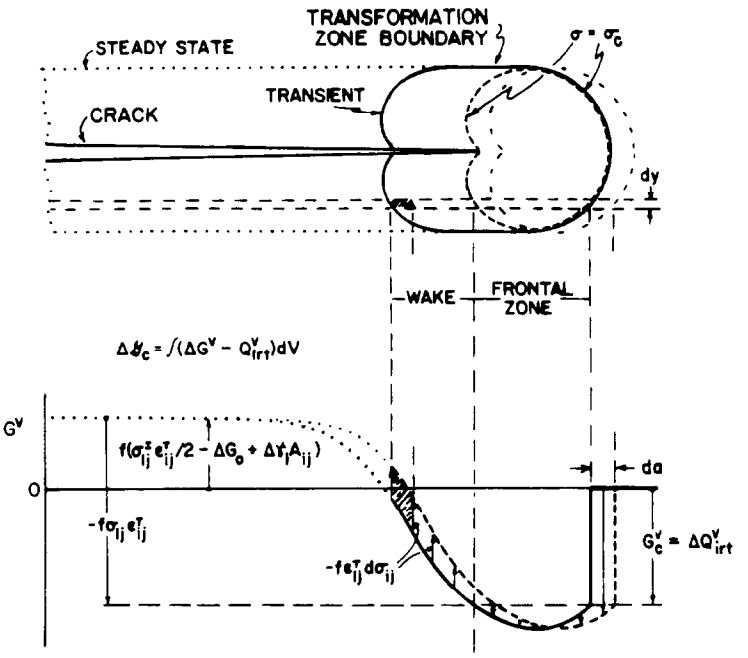

Fig. 19. Variation in free energy with position relative to the crack tip and the effect of crack advance on the net energy change.

material can be analyzed in terms of the interaction stresses by noting that

$$dE^v = dQ^v_{ir} + TdS^v + \sigma_{ij}d\varepsilon'_{ij} \qquad (6.28)$$

where E is the excess internal energy (with the superscript v denoting energy density or heat generation per unit volume), and $d\varepsilon'_{ij}$ are the inelastic strain increments. Moreover, the toughness analysis is facilitated by recognizing that the effect of an increment of crack advance may be associated with moving elements from far ahead of the crack, through the high stress field and into the wake (Fig. 19), and that at steady state this motion into the far wake leaves U_l unchanged.

If the transformation reverses (in the wake) with passage of the crack, then the transformed volume does not change during steady state propagation, and the toughening derives entirely from heat generation associated with moving the zone. Integration around the stress–strain curves for a loading–unloading cycle gives $\Delta E^v = \Delta G^v = 0$, and the resultant asymptotic toughness as

$$\Delta\mathscr{G}_c = 2\int_0^h \left\{\int_0^{\varepsilon_m} (\sigma^f_{ij} - \sigma^b_{ij})d\varepsilon_{ij}\right\} dy \qquad (6.29)$$

where σ^f_{ij} and σ^b_{ij} are the interaction stresses for forward and reverse transformation [55, 34]. The differences in these stresses determines the zone depth, and their magnitudes control how far the zone is displaced back relative to the equilibrium zone (which causes the net closure forces that give ΔK).

If the transformation does not reverse after crack passage, then the toughness results from heat generated at the zone front, and from the increased free energy stored in the wake (since $dV/lda = 2h$). For steady state, the pertinent energy changes may, again, be related to the loading and unloading stress–strain curves of individual elements (Fig. 20), such that

$$\int \sigma_{ij}d\varepsilon'_{ij} \equiv U^v_c = +U^v_0 - f\Delta G_0 + f\Sigma\Delta\gamma_i A_{vi} - \Delta Q^v_{ir}. \qquad (6.30)$$

Thus, from equations (6.30) and (6.27), the toughness is conveniently expressed in terms of the interaction energy, as

$$\mathscr{G}_c = 2\int_0^h \left\{\int_0^{f\varepsilon^T} \sigma_{ij}d\varepsilon_{ij} + \int_0^{\sigma^r} C_{ijkl}\sigma_{ij}d\sigma_{kl}\right\} dy \qquad (6.31)$$

where C_{ijkl} is the elastic stiffness tensor. The first integral is taken over the loading portions of the set of stress–strain curves and then down the unloading segments back to zero stress. The second integral†

†The second term arises because some of the strain energy accounted in G, expressed using the Eshelby formulation [equation (4.1)], is outside the transformed particle. This integral pertains to that energy outside the element of particles and matrix and allows the volume integral to be taken simply over the zone. Also note that if the transformation zone is small (about one particle diameter in width), $U_0 \sim 0$ at low f, because the crack surface relaxes the transformation strain. Then, U_0 would be eliminated from the expression for $\Delta\mathscr{G}_c$ but the contribution from the energy expended to initiate transformation would remain. (However, in the absence of dissipation, this would give $\Delta\mathscr{G}_c \simeq -\Delta G_0$ which is negative.)

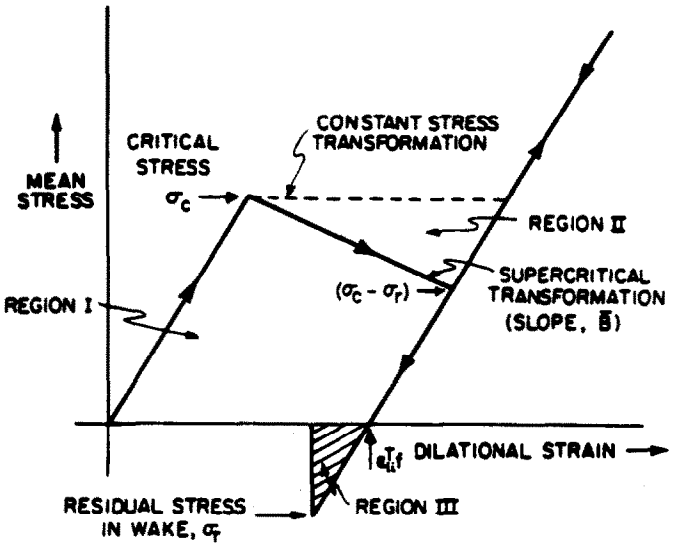

Fig. 20. A schematic stress–strain curve for the supercritical martensite transformation, indicating the critical stress and the permanent strain.

corresponds to that portion of the residual strain energy associated with the residual stress imposed by the surrounding material (region III, Fig. 20). This expression is independent of the balance of stored energy and dissipation. However, the ΔQ_{ir} term in equation (6.27) is usually expected to be dominant.

An interaction energy analysis was originally done for a dilational transformation [34]. With the simplifying assumption that supercritical transformation occurs under constant stress (see later), the steady state toughness obtains as

$$\Delta \mathscr{G}_c = 2f\varepsilon_{ii}^T \bar{\sigma}_c h. \tag{6.32}$$

By making the association that the critical stress is related to the zone height, [equation (6.10)] and recalling that, $K^2/E(1-\nu^2) = \mathscr{G}$, it has been demonstrated‡ that $\Delta \mathscr{G}_c$ given by equation (6.32) is *identical* to ΔK_c predicted by equation (6.12).

The existence of an R-curve is also predicted, because the increments of transformed material added at the rear of the zone have successively higher G^v, owing to the reduced crack field stresses and associated interaction energies, $\sigma_{ij}\varepsilon_{ij}^T$ (Fig. 19). Curiously, even though dissipation is occurring at the onset of propagation, the toughness is zero, at least when the zone shape is controlled by a critical mean stress.† This seeming paradox results from a balance of the dissipation at the zone front and strain energy reduction at the rear. This balance obtains because, at the onset of extension, the frontal zone shifts forward by transformation at the front, generating heat and leaves behind an increment of previously transformed material at the rear. The material initially "deposited" in the wake satisfies $G^v = \Delta Q^v_{irt}$, as is evident from equation (6.23) and from recognizing that, at the prior instant, dissipation was occurring at the front *and* rear of the zone. Because of this balance the toughening has been viewed solely in terms of the interaction energy behind the frontal zone [34].

(*ii*) *Energy balance integrals.* Analogous results can be derived by examining energy balance integrals [10]. For the frontal zone (Fig. 14), the volume elements within the transformation zone do not experience unloading. Consequently, the path-independent J-integral applies, and the relation

$$J = (1-\nu^2)K^2/E \tag{6.33}$$

pertains for all line contours around the crack tip. Furthermore, since the elastic properties of the transformed and untransformed materials are essentially the same, contours around the tip (giving K_{tip}) and remote from the tip (giving K_∞) yield identical values of K: whereupon $K_{tip} = K_\infty$.

Conversely, when a fully developed zone exists (Fig. 14), the material within the zone, behind the crack tip, has experienced unloading and a path independent J does not apply. In this case the appropriate energy balance integral, I, has the same form

‡This is only direct for the small strain approximation. However, using more rigorous relations obtained with energy balance integrals [equation (6.36)] it has been shown [10], Fig. 21, that the $K - \sqrt{h}$ relationship is obeyed well for larger ΔK, where equation (6.10) overestimates h.

†This balance results if the interaction energy, $\sigma_{ij}\varepsilon_{ij}^T = \bar{\sigma}\varepsilon_{ii}^T$, controlling G^v at the rear equals $\int \sigma_{ij} d\varepsilon'_{ij}$ at the front. This condition obtains with pure dilation, only if the front and rear boundaries are dictated by the same $\bar{\sigma}_c$. The balance of dissipation and reduced strain energy giving $\Delta \mathscr{G}_c = 0$ at the onset of crack extension can be satisfied for certain other transformations involving shear. One criterion which would identify such transformations requires a transformation law wherein the initial loading zone has the same shape and population profiles as that for an equilibrium traveling crack [27, 39].

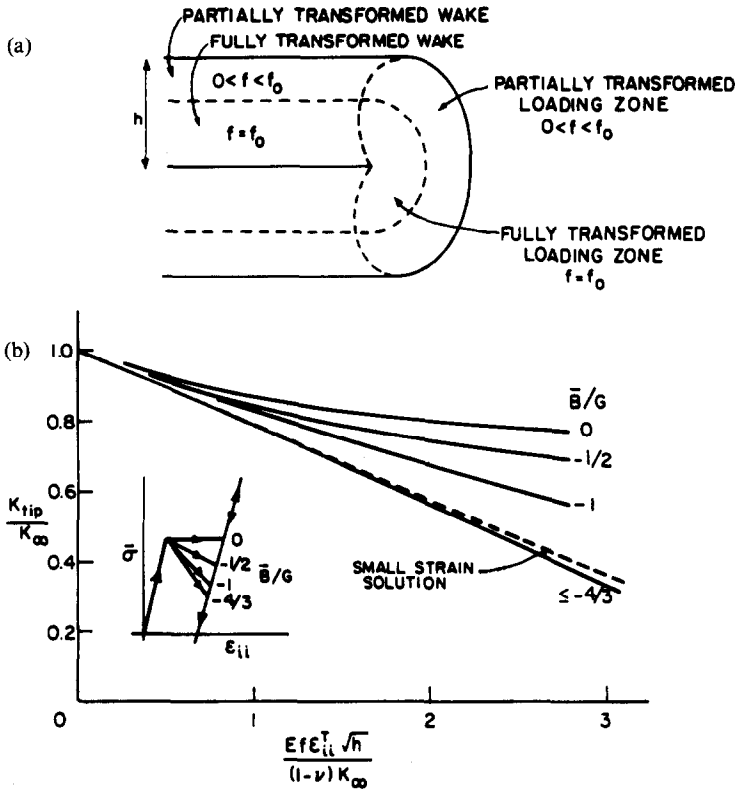

Fig. 21. Steady-state transformation zones and toughening for subcritical transformations (Ref. [10]): (a) the fully transformed inner zone and partially transformed outer zone, (b) ratio of near-tip to remote stress intensity factors for subcritical stress–strain curves with dilational coupling. The dashed line is the analytical result for small $f\varepsilon_{ii}^{T}$.

as J at the tip

$$I = (1-\nu^2)K_{tip}^2/E \tag{6.34}$$

but remote from the tip becomes [10]

$$I = (1-\nu^2)K_{\infty}^2/E - 2\int_0^h U^v(y)\,dy \tag{6.35}$$

where $U^v(y)$ is the residual energy density in the wake. Equating the magnitude of the conservation integral for the near-tip and remote paths, thus, gives

$$K_{\infty}^2 = K_{tip}^2 + [2E/(1-\nu^2)]\int_0^h U^v(y)\,dy \tag{6.36}$$

or†

$$\Delta\mathscr{G}_c = 2\int_0^h U^v(y)\,dy \tag{6.37}$$

†Comparison of equation (6.37) with equation (6.31) indicates that $U^v(y)$ is related to the interaction energy. In fact, the determination of $U^v(y)$ involves procedures similar to the interaction energy calculations.

‡The solution for $\Delta\mathscr{G}_c$ determined from the interaction energy change based on "prior" stresses may have seemed fortuitous because the supercritical transformation does not occur at constant average stress. However, the energy deficit accompanying the stress drop during transformation (region II in Fig. 20) is exactly offset by the stored strain energy in the wake (region III in Fig. 20) [54].

The evaluation of $U^v(y)$ can be conducted rigorously by relating $U^v(y)$ to features of the stress–strain curve (Fig. 20). It is recognized that the material in the wake undergoes a complete loading and unloading cycle as the element translates from the front to the rear of the crack tip during crack advance. Hence, each element in the wake is subject to the residual stress work contained by the hysteresis loop (Fig. 20). Consequently, by appreciating that the wake is subject to a residual compression, due to transformation (Fig. 20), given by [10]

$$\sigma_{11} = \sigma_{33} = Ef\varepsilon_{ii}^{T}/3(1-\nu) \tag{6.38}$$

the residual energy density can be readily evaluated as [10]

$$U^v(y) = \sigma_c\varepsilon_{ij}^{T}f + \frac{\bar{B}(\varepsilon_{ii}^{T}f)^2}{2(1-\bar{B}/\beta)} + \frac{E(\varepsilon_{ii}^{T}f)^2}{9(1-\nu)} \tag{6.39}$$

where $\bar{B}$ is the slope of the stress–strain curve of the transforming material (Fig. 20). The three terms in equation (6.39) derive from the areas I, II and III under the stress–strain curve depicted in Fig. 20. The latter two terms cancel when

$$\bar{B} = -2E/3(1+\nu) \tag{6.40}$$

and equation (6.39) for the toughening is then *identical* to equation (6.32).‡ The above condition for $\bar{B}$

has been determined to obtain at the *supercritical* condition [10].

6.4. Sub-critical transformations

The preceding discussion has referred exclusively to supercritical transformations, wherein all particles within the zone exhibit transformation. Such behavior is only observed in PSZ. More generally, subcritical transformation occurs, whereupon only a fraction of the parent phase transforms. Sub-critical transformations are characterized by a transformation slope [10] $d\bar{\sigma}/d\varepsilon_{ii} > -4\mu/3$ (Fig. 21). Furthermore, specification of the slope, allows the zone size and the extent of transformation within the zone to be evaluated and thereby, related to the toughness. Some typical results determined numerically [10] for the dilatational transformation are plotted in Fig. 21. In these instances, the overall transformation mechanism is important, in the sense that the shape of the stress–strain curve is dictated by the nucleation, growth, and twinning characteristics of the martensite.

Alternatively, sub-critical toughening can be characterized in terms of the distribution of transformed particles $f(y)$ as a function of the distance y from the crack plane. This formulation is particularly useful because $f(y)$ can be determined experimentally [28] (Section 10). The solutions can be straightforwardly evaluated from the supercritical transformation solutions by considering the contribution to ΔK from each part of the distribution, df [9]. For example, the net ΔK_c for the dilatational transformation is

$$\Delta K_c = \left\{[0.22 E\varepsilon_{ij}^{T}/(1-\nu)] \int_h^0 \sqrt{y}\left(\frac{df}{dy}\right) dy\right\}. \quad (6.41)$$

6.5. R-curve effects

When the transformation zone extends into the wake by a distance $\Delta a < 5h$, the ΔK is less than the asymptotic value. R-curve behavior is thus predicted in this range, as illustrated in Fig. 14. Such effects are only expected, of course, when the zone wake evolves during crack extension. Furthermore, the slope of the R-curve has only been explicitly predicted [9, 34] for the dilatational transformation and for small ΔK, whereupon widening of the zone during crack advance is unimportant. The effects of shear require further investigation. However, energy arguments suggest that for certain situations wherein† the transformation strains that control the zone shape during loading are the same as the net transformation strains, then the initial $\Delta\mathscr{G}_c$ should be zero, whereupon, large R-curve effects are anticipated. Conversely, where the stress components controlling the zone shape are not those that couple with the net transformation strains, the initial ΔK is expected to be nonzero resulting in reduced R-curve tendencies. Significant resistance curve effects have been experimentally observed, as elaborated in Section 10.

6.6. The influence of reversibility

The preceding analysis of toughness has implicitly assumed that the transformation, once activated, does not reverse when the stress is released in the crack wake. However, it is important to note that substantial toughening can still obtain when the reverse transformation is allowed [55]. The associated behavior is readily perceived by utilizing the stress–strain curve developed in Section 6.3. The most illuminating example considers the stress–strain curve depicted in Fig. 22, wherein the transformation fully reverses (supercritically) at an applied stress infinitesimally larger than zero. For this case, all of the stress–strain hysterisis is utilized, except possibly for part of the compression in the remote wake.‡ The toughness should thus approach that attributed to the irreversible transformation. The specific level of toughness, ΔK_c, can be evaluated straightforwardly using the zone profile (Fig. 22) in conjunction with equation (6.6). This procedure reveals that, for the dilatational transformation

$$\Delta K_c \simeq 0.20\, Ef\varepsilon_{ii}^{T}\sqrt{h}/(1-\nu). \quad (6.42)$$

Alternatively, it is easily shown that for supercritical reversal at vanishing stress, as in Fig. 22, all the strain energy stored in *and* around the retained zone is dissipated as unrecoverable work during release of the residual compression. Thus, the total hysteresis energy $U^{v}(y)$ and the resultant $\Delta\mathscr{G}_c$ are identical with those for the unreversed case. More generally, for a final reversal stress, δ, the equivalent expression for ΔK_c is

$$\Delta K_c = 0.22\, Ef\varepsilon_{ii}^{T}(1-\delta/\sigma_c)\sqrt{h}/(1-\nu). \quad (6.43)$$

Consequently, when the transformation reverses to give zero final stress, the toughness may be nearly identical with that for the supercritical, unreversed case.

The importance of this result can be appreciated by realizing that the entire transformation zone would fully reverse when the applied loads are removed, because the transformed zone is in residual compression. Hence, a zone would not be observed using the usual observational techniques [6, 28, 56] (TEM, X-rays, Raman scattering, etc.), because they are generally applied after load removal. Only *in-situ* measurements would reveal the full extent of the

†These are situations for which the loading zone would be identical to that for the traveling crack with no dissipation. The calculations [50] based on relaxed shear stress [equations (5.15) and (5.20)], which gave initial $\Delta K < 0$, (Section 6.2) seem not to satisfy this criterion because the equilibrium zone should be subcritical and the stresses in the partially transformed particles should not be fully compensated. Moreover, those calculations did not limit the shear, leading to high strains near the tip and finite ΔK at negligible zone widths.

‡To fully understand the toughening, it is helpful to recognize that although the applied stress in the remote wake is small, the actual stress-strain hysteresis includes a contribution from dissipation of this residual compression imposed by the untransformed surroundings.

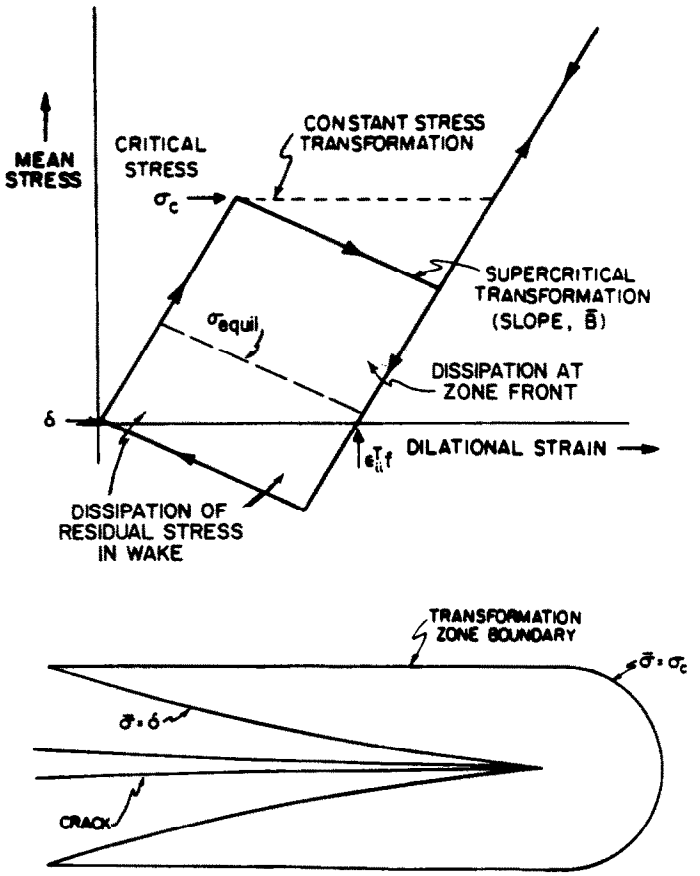

Fig. 22. Stress–strain curve and associated transformation zone for a reversible transformation.

zone. Caution must, therefore, be exercised when using zone size and shape measurements to interpret trends in toughness, as discussed in Section 10.

6.7. The toughness

It is readily appreciated from the preceding analysis that transformation induced toughening increases as the transformation zone size increases, or equivalently, as the critical stress decreases. It is pertinent here to discuss the trends in transformation toughening that arise from corresponding trends in the critical stress, as a basis for interpreting experimental observations.

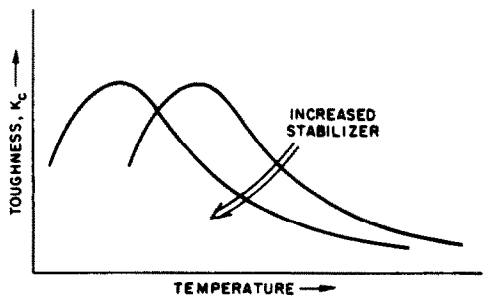

Fig. 23. Schematic trends in K_c with temperature and solute content.

The stress controlling the zone dimensions is imprecisely understood. However, the critical stress, as dictated by the nucleation condition, can be reasonably supposed to diminish with supercooling, and to approach small values at temperatures just above M_s. Consequently, K_c must increase as the temperature decreases (Fig. 23), as is commonly observed. At temperatures below M_s, the thermally transformed material does not contribute to crack shielding (i.e. does not result in a long range residual compression over the crack surface). Hence, K_c must diminish, as depicted in Fig. 23. The toughness is also modified by the presence of solute (Fig. 24), consistent with the solute effect on σ_c and M_s. Finally, the M_s temperature is influenced by particle size and shape, such that larger or more angular particles exhibit larger M_s temperatures. Trends with particle size and shape can again be predicated on the analagous trends in M_s, as summarized in Fig. 25 and illustrated in Fig. 26.

The preceding calculations reveal explicit effects on the toughness of the transformation strain tensor and zone shape, as reflected in the coefficient on $Ef\epsilon_{ii}^T\sqrt{h}$ (Table 1). Comparison of the two cases for which the transformation is irreversible and purely dilational reveals an important effect of *zone shape*. Notably, the toughness is increased by a factor of 1.7 by eliminating a frontal segment. A comparable effect

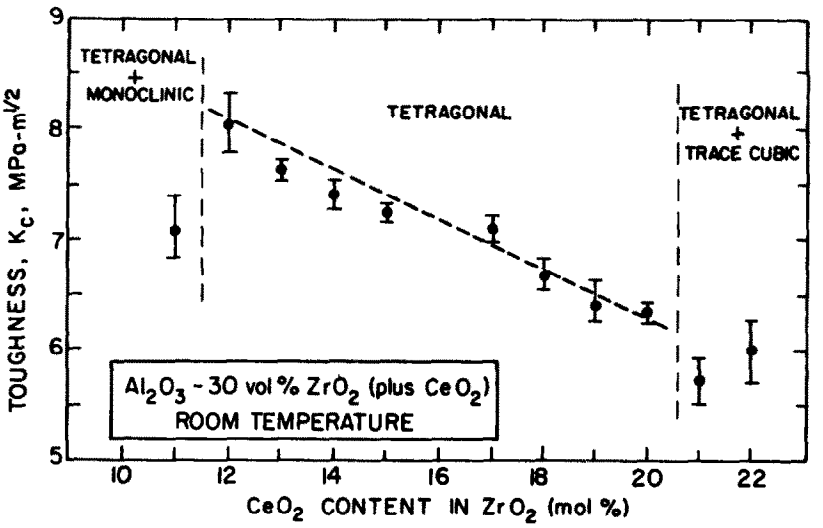

Fig. 24. Fracture toughness for Al_2O_3–ZrO_2 materials vs CeO_2 stabilizer content in the ZrO_2 (Ref. [3]).

of *strain tensor* is contained in the result for uniaxial dilation. In this instance, the calculated zone front is only partially flattened, and thus the deviatoric strains are predominantly responsible for the additional toughness. However, it should be recognized that extensive twinning may limit the net deviatoric transformation strain and the resultant toughening. The transformation strain tensor may also influence the zone size, which, in turn, can enhance the toughness under suboptimal conditions. This behavior is clearly illustrated in Fig. 27, wherein the zone sizes and shapes derive from the crack tip stresses required to satisfy a critical nucleation condition [equation (4.7)].

A sample size effect exists at low critical stresses (Fig. 28), because the zone begins to extend spontaneously and diminishes the closure forces on the crack. Spontaneous spreading is expected to occur when the zone size attains some fraction ($< 1/2$) of the sample size, as dictated by the chemical driving force, the net transformation strains within the zone, and the far field stresses (and hence, by the crack size). The optimum toughness thus occurs at temperatures for which the zone size approaches a fraction of the sample size.

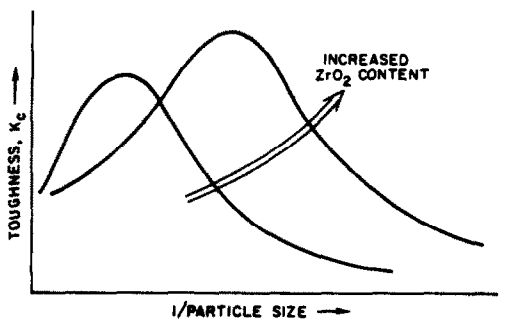

Fig. 25. Trends in K_c with particle size and concentration.

In many instances, significant toughening persists to (or above) the equilibrium transformation temperature, T_0. At this temperature, the high residual strain energies far exceed the chemical driving force but the very large crack tip stresses still provide an impetus for transformation. The residual stresses then cause reversal of the transformation, but hysteresis is necessarily involved and causes toughening.

In closing, a cautionary note regarding the available ΔK calculations is deemed appropriate. Calculations which assume a net deviatoric transformation strain yield a small, nonzero shielding prior to propagation. More importantly, calculations based on shear band boundaries predict appreciable initial toughness, as well as higher steady-state toughness.

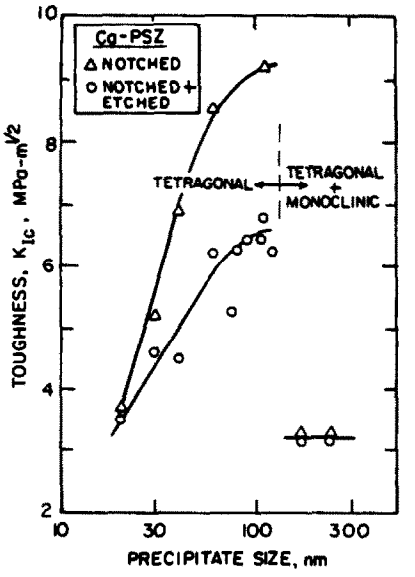

Fig. 26. Influence of precipitate size on the fracture toughness for CaO/PSZ after various heat treatments (Ref. [6]).

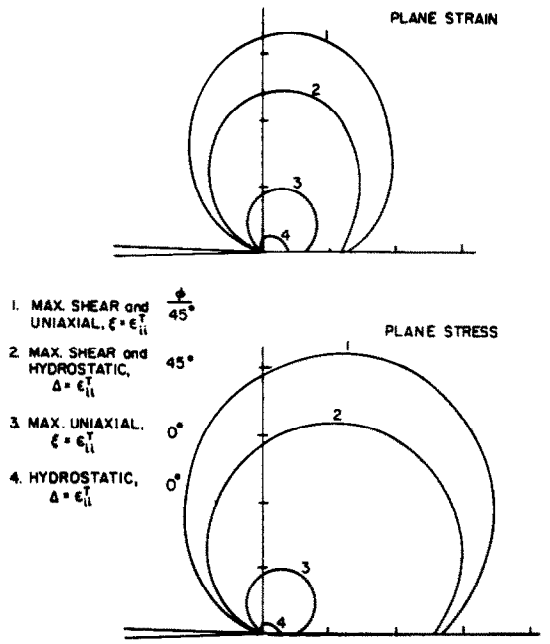

Fig. 27. Transformation zone boundaries defined by crack tip nucleation stresses, with various types of stress coupling at constant remote intensity. The stress coupling depends upon the embryo orientation relative to the maximum principal stress, angle ϕ between σ_{11} and the particle normal, and the transformation strains. The examples of ε_{ij}^T are invariant plane strain, $\xi = \varepsilon_{ii}^T$, with a lattice shear and isotropic dilation, $\Delta = \varepsilon_{ii}^T$, plus a lattice shear. (courtesy T. W. Coyle).

This behavior apparently obtains because the J-integral is path dependent, whereupon the zone size and shape are controlled by condition near the *cracktip*. Comparable effects on initial and steady state K could be anticipated if the zone boundaries were controlled by a nucleation conditions not based on the net transformation strains. Such situations may be physically realistic, but care is required to assure correspondence between physically possible and calculated configurations.

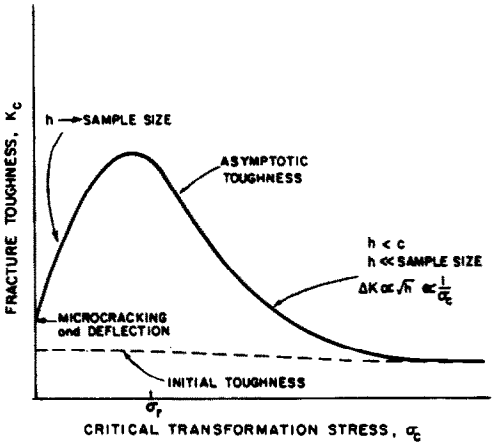

Fig. 28. Schematic illustrating expected trends in K_c with critical transformation stress for initial and asympotic toughnesses. The initial toughening arises from deflection.

7. MICROCRACK TOUGHENING

The transformation induces residual tensile stresses that may, in turn, initiate microcracks. Such microcracks are capable of enhancing toughness [57–59]. Experience indicates that microcrack nucleation becomes more probable as the scale of the residual field increases [43, 60]. The presence of large stress concentrations, at corners, is also conducive to the nucleation process. Microcracks are thus deemed most likely in the presence of intergranular particles with large facet lengths, such that the cracks form in the matrix between neighboring particles. Furthermore, matrix grain boundaries are particularly susceptible to microcracking [5, 57, 61].

Microcracks invariably form in regions of residual tension. Relief of this residual stress by the microcrack results in residual opening, and associated dilatation [58]. The dilatation is the prime source of microcrack toughening [58, 59], analagous to the role of dilatation in transformation toughening. The extent of the dilatation can be estimated provided that

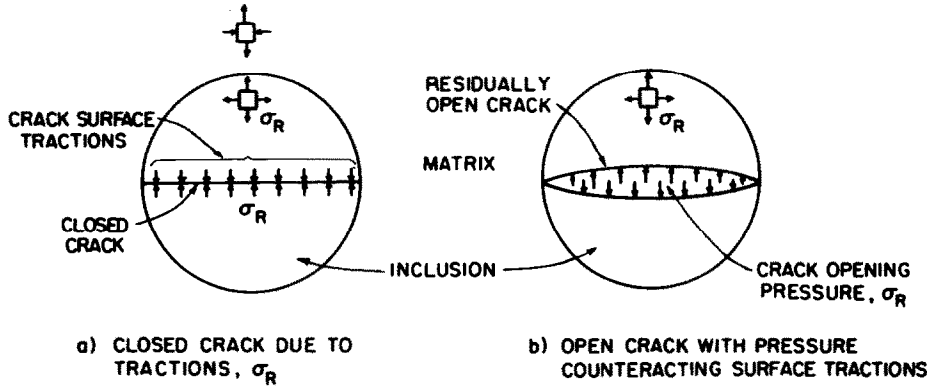

Fig. 29. Schematics illustrating geometry and successive operations used to deduce the toughening for cracked particles.

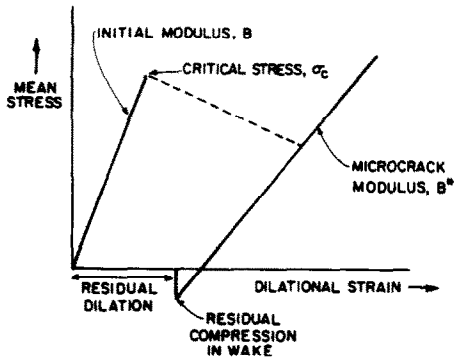

Fig. 30. A schematic stress–strain curve for supercritical stress induced microcracking of particles.

prior residual tension on the microcrack plane is known. This possibility is illustrated for spherical regions that microcrack across their center [59]. The extent of residual crack opening that accompanies microcracking can be visualized by firstly emplacing the crack across the sphere while imposing surface tractions equal to the residual stress, σ_R, in order to maintain contact of the crack surfaces (Fig. 29). Then, a pressure of magnitude σ_R is applied inside the crack, to create the stress free microcrack surfaces. This step induces a crack opening identical to that experienced by an initially stress free solid, because elastic deformation is linear and the stresses are additive. Furthermore, the opening displacement of a pressurized crack is the same as that for a crack subject to a remotely applied uniform tension of equal magnitude [62]. The residual microcrack opening is thus precisely the same as that experienced by a crack subject to an applied stress equal to the residual stress. Hence, solutions for the *bulk modulus*, B^*, of microcracked solids [63] give a direct prediction of the dilatation in terms of σ_R. For example, the volumetric strain induced by non-interacting microcracks is simply [59]

$$\varepsilon_{ii}^c = \frac{16(1-\nu^2)}{3}\frac{\sigma_R f}{E_0} \tag{7.1}$$

where f is the volume fraction of microcracked spherical particles and E_0 is the modulus for the uncracked material.

The dilatation, ε_{ii}^c, can be used to predict the toughness by adopting the line integral procedure developed for transformation toughening, equation (6.36). For illustrative purposes, a simplified constitutive law is used, as required to demonstrate the essential trends. It is assumed that the microcracks are isotropic and form in response to the *mean stress*, at a critical value σ_c', and that the microcracked material has a reduced modulus, B^* (Fig. 30). Furthermore, since fracture occurs when K_{tip} attains the toughness of the *microcrack degraded* material, it is assumed that the degradation has the form [58]

$$K_{tip} = K_0(1-f). \tag{7.2}$$

The change in toughness for this isotropic process can then be demonstrated to exhibit the form

$$\Delta K_c = 0.21\, E_0\, \varepsilon_{ii}^c \sqrt{h}/(1-\nu). \tag{7.3}$$

Incorporating ε_{ii}^c from equation (7.1), the toughness for a system containing noninteracting cracked spheres can be expressed as [59]

$$\Delta K_c = 1.12(1+\nu)\,\sigma_R f \sqrt{h}. \tag{7.4}$$

The analagous result if microcracks respond to the *principal tensile stress* (instead of the mean stress) is [59]

$$\Delta K_c = 2.67\,\sigma_R f \sqrt{h}. \tag{7.5}$$

The preceding solutions, although not strictly applicable to ZrO_2 toughened systems (which exhibit matrix microcracking), provide several useful insights by virtue of their simplicity. Specifically, independent estimates of the residual stress and zone width may be used to assess the general magnitude of microcrack toughening, compared with transformation toughening. For example, in ZrO_2 containing systems, since $\sigma_R \approx \sigma_{ii}^I \varepsilon_{ij} = (2/9)E_0 \varepsilon_{ii}^T/(1-\nu)$, comparison of equation (7.4) with equation (6.12) reveals that, for the same process zone width, h, the transformation and microcracking mechanisms are comparably effective.

Further progress in understanding microcrack toughening in ZrO_2 systems requires solutions of the analagous *matrix* microcracking problem. A preliminary attempt is illustrated in Figs 31 and 32. Initially, simultaneous transformation and microcracking of tetragonal ZrO_2 is considered. To address this problem, matrix cracks are presumed to extend fully across the volume element between adjacent

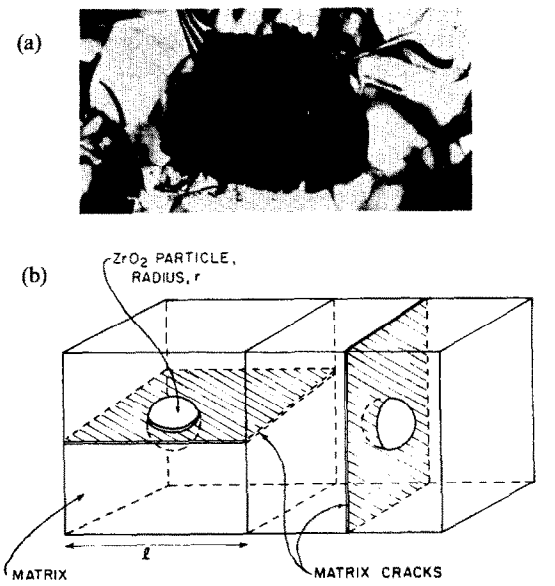

Fig. 31. (a) Matrix microcracking in ZTA material (courtesy M. Rühle). (b) Schematic of idealized microstructure for noninteracting matrix cracks extending across the volume element between particles.

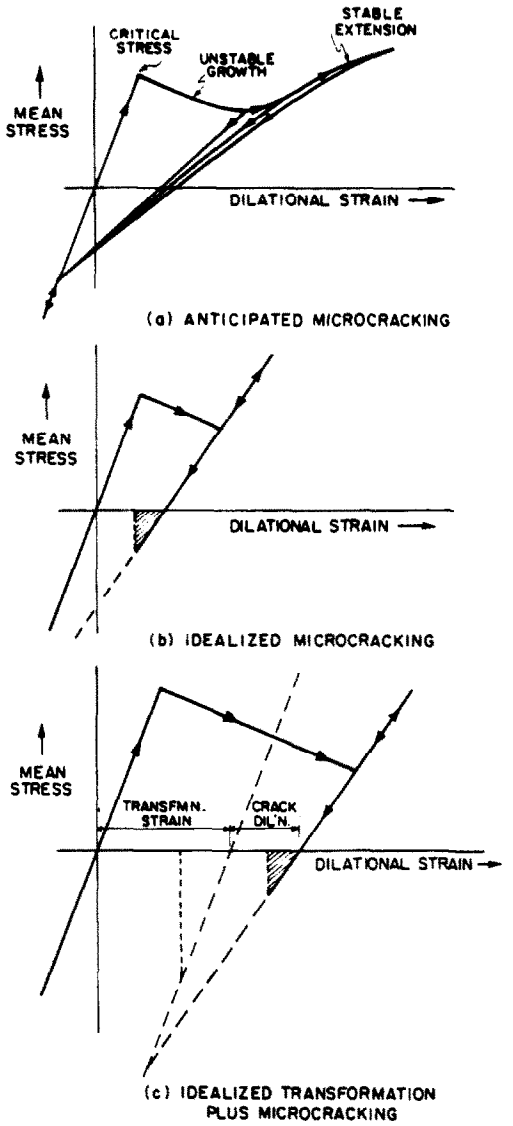

Fig. 32. Schematic of stress–strain curves for material undergoing simultaneous transformation and matrix microcracking. Although subcritical behavior may be anticipated during the late stages of crack growth, supercritical behavior controlled by the critical transformation stress is assumed for the calculations.

ZrO_2 particles [64]. The volumetric strain experienced by each microcracked element is then

$$\varepsilon_{ii}' = (2\varepsilon_{ii}^T/3)\,(f + r/l) \qquad (7.6)$$

where r is the ZrO_2 particle radius and l is the dimension of the element. Hence, by noting that, $r/l = (3f/4\pi)^{1/3}$, the change in asymptotic toughness for isotropic microcracking (equation 7.3) becomes

$$\Delta K_c = \frac{0.14}{(1-\nu)} E_0 \varepsilon_{ii}^T \sqrt{h}\,(f + 0.6 f^{1/3}). \qquad (7.7)$$

The corresponding result for microcracking of pretransformed but uncracked material is

$$\Delta K_c = \frac{0.07}{(1-\nu)} E_0 \varepsilon_{ii}^T \sqrt{h}\,(1.2 f^{1/3} - f). \qquad (7.8)$$

Comparison with transformation toughening [equation (6.12)] suggests the interesting result that, for equivalent process zone widths, simultaneous transformation and microcracking imparts more effective shielding than transformation alone. In turn, transformation shielding is more effective than microcrack shielding in pretransformed material (Fig. 33). This effect is most pronounced at small volume concentrations of particles, due to the additional $f^{1/3}$ term. This difference in dependence on f obtains because the microcracks are considered to occur in the matrix *between* ZrO_2 particles such that, microcracking becomes relatively larger in extent as f diminishes. However, in attempting comparison with transformation toughening, it should be recalled that ΔK_c is superimposed upon a degraded toughness [equation (7.2)] which counteracts the enhanced ΔK_c, especially at larger f. Nevertheless, microcrack associated toughnesses in ZTA of ~ 10 MPa-m$^{1/2}$ (Section 10) reveal that microcrack toughening can be significant.

Finally, it is noted that R-curve effects are also expected for microcracking processes [58]. The R-curve behavior obtains in this instance, even though the frontal zone provides some shielding, because the shielding is fully counteracted by the crack tip degradation. Such increases in toughness with crack advance have been observed for overaged PSZ (Section 10).

Relations between h and the critical stress for microcracking, σ_c', are analogous to those for transformation toughening. Specification of σ_c' is no better understood than for the critical transformation stress [32] and is comparably important. The critical stress depends on the flaw population around the particles and upon microcrack nucleation in the high stress fields near corners or twin intersections. Thus,

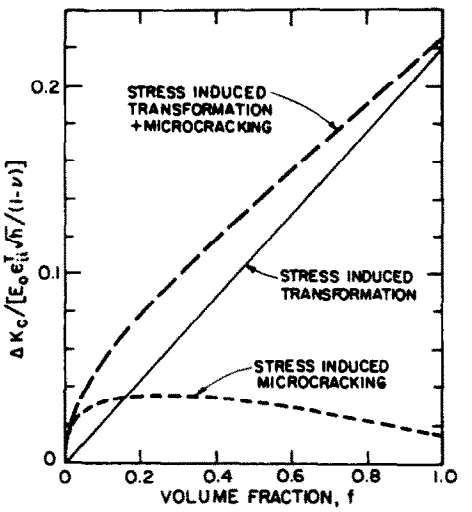

Fig. 33. Comparison of normalized K_c vs volume fraction of particles for shielding by stress induced transformation, transformation plus microcracking, and stress induced microcracking in pretransformed material.

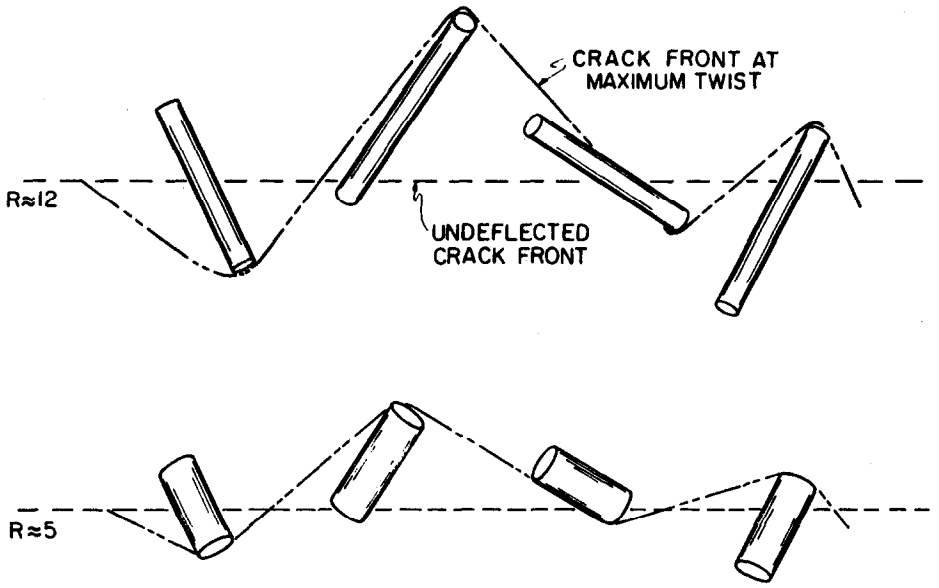

Fig. 34. Schematics showing critical configuration for twist of a crack around rods of two aspect ratios, R, at constant volume fraction.

significant effects of sample density and particle location are anticipated.

8. CRACK DEFLECTION TOUGHENING

Cracks can be deflected either by localized residual fields or by fracture resistant second phases [65]. The deflection results in a toughening dictated by the reduced driving force on the deflected portion of the crack. A reduced driving force obtains on both tilt and twist crack front segments, although the twisting of the crack (Fig. 34) generally provides the larger reduction [65]. The net driving force on a small deflected segment of a crack can be estimated by separately evaluating the modes I, II and III strain energy release rates. This is achieved by determining the normal and shear stresses on the plane of the perturbation relative to the principal crack and evaluating the stress intensity factor. On a twisted segment, for which the modes I and III contributions are of primary concern, this procedure yields [65]

$$K_I/K_\infty = k_{11}(\phi)\cos^3(\theta/2) + k_{12}\sin(\theta/2)\cos^2(\theta/2) \quad (8.1)$$

$$K_{III}/K_\infty = k_{31}(\phi)\cos^3(\theta/2) + k_{32}(\phi)\sin(\theta/2)\cos^2(\theta/2) \quad (8.2)$$

where θ is the maximum tilt and ϕ is the corresponding twist of the perturbation front and k_{ij} are the functions plotted in Fig. 35. The deflection angles are functions of the volume fraction and shape of the deflecting particles. For a given volume fraction of particles, the largest deflection angles obtain in the case of rods [65]. Discs produce intermediate deflection, while spheres induce the least. The specific

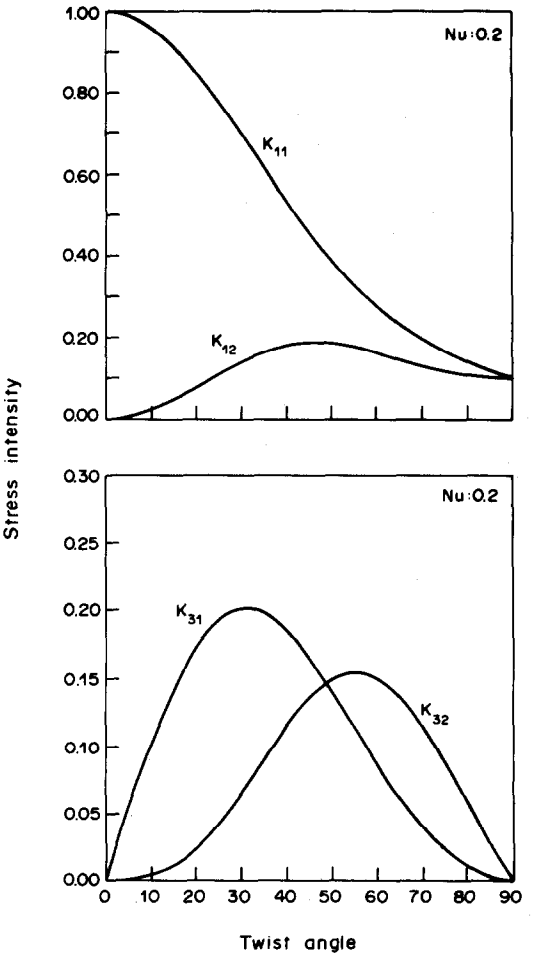

Fig. 35. Angular functions k_{11}, k_{12}, k_{31} and k_{32} vs twist angle, $\theta = \phi$, for the functions used to modify the local stress intensity factors, K_I and K_{III} (Ref. [65]).

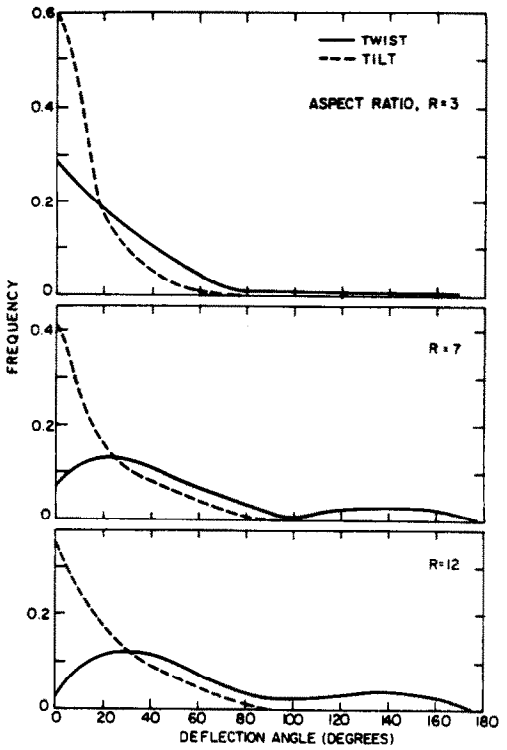

Fig. 36. Frequency distributions for average twist and tilt angles intercepted by a normal plane for randomly oriented rods of three aspect ratios, present in volume fractions of 0.2 (Ref. [65]).

angular range associated with the deflection process can be deduced by considering the distribution of angles between the end of the particles in a random array. Some typical angular distributions for rods are summarized in Fig. 36. These angles may be incorporated into equations (8.1) and (8.2) to deduce the K_I, and K_{III} distribution along the crack front. A crack growth hypothesis is then needed to predict the extent of toughening. Available studies [65] have assumed that both the normal and shear stresses fully couple with the crack growth mechanism (provided that $K_I > 0$), such that a perturbed segment of the crack front grows along its original plane of deflection, subject to

$$K_I^2(1-\nu^2) + K_{III}^2(1+\nu) \geqslant E\mathscr{G}_0 \qquad (8.3)$$

where $\mathscr{G}_0$ is the matrix crack growth resistance. This criterion provides the minimum deflection toughening. Reduced coupling of K_{III} to the fracture mechanism (as obtains, for example, in the delamination of composite plates [66]) would result in larger toughness. The fully coupled shear criterion results in a net crack front driving force, integrated over all deflection angles, that increases the toughness to the extent summarized in Fig. 37. Most of the toughening develops in the range $f \leqslant 0.2$, for all particle shapes and, as expected, strong aspect ratio effects pertain for rods and discs [65].

Fractography usually reveals rough fracture surfaces for materials containing monoclinic ZrO_2 indi-

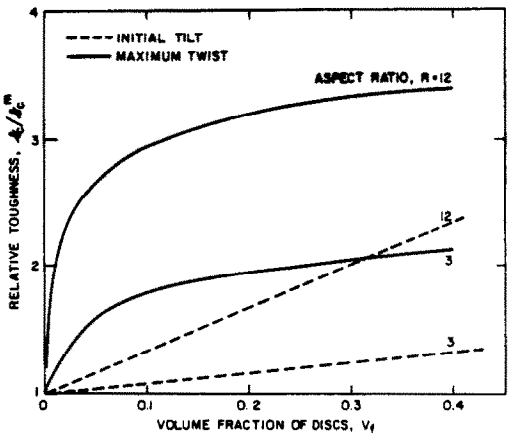

Fig. 37. Relative toughness predictions for initial tilt and for maximum twist based on crack deflection model for disc-shaped particles of two aspect ratios. These illustrate the greater effect of twist especially at low concentrations (Ref. [65]).

cating an important deflection contribution to the toughness [18]. Both TEM and SEM examination indicate that cracks usually deflect or branch in attempt to avoid monoclinic particles in the transformation zone [18, 19], whereas, tetragonal particles (e.g. for substantially underaged PSZ), reportedly do *not* influence fracture morphology [6]. Similar behavior was indicated for a series of ZnO–ZrO_2 alloys [67], containing monoclinic or Y_2O_3 stabilized tetragonal ZrO_2, wherein the toughness was found to depend primarily on the monoclinic content (Fig. 38). The deflection apparently arises as a consequence of the residual stress fields associated with the monoclinic phase.

The morphology of the precipitates in MgO/PSZ materials indicates that disc solutions are most pertinent (aspect ratio ~ 5). However, the present solutions [65] are restricted to randomly oriented discs, whereas, the orientations in PSZ are nonrandom [18]. The substantial proportion of high twist angles apparent in PSZ (Fig. 39) suggests that deflection

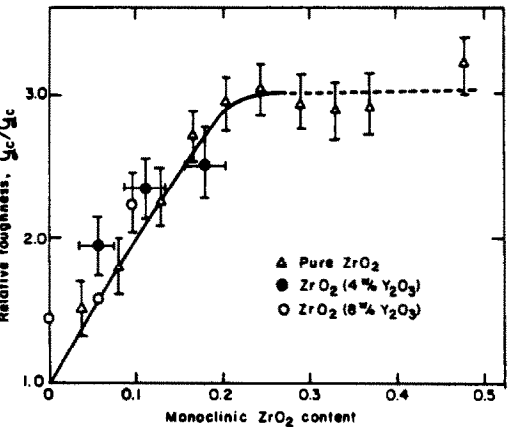

Fig. 38. Relative toughness versus monoclinic ZrO_2 content measured in ZnO–ZrO_2 alloys (Ref. [67]).

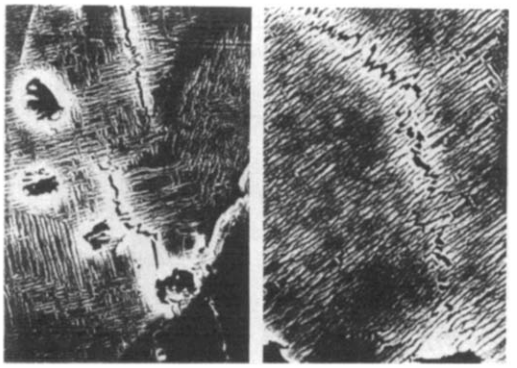

Fig. 39. Scanning electron micrographs of cracks interacting with coarse, intragranular precipitates in overaged MgO/PSZ (courtesy M. V. Swain).

toughening in this material should exceed predicted levels ($K_c/K_0 \simeq 1.5$). Further study is needed to examine this possibility. In ZTA and CaO/PSZ the precipitates are essentially equiaxed, and deflection toughening levels based on spheres should apply ($K_c/K_0 \approx 1.3$, Fig. 40). However, it is noted that the deflection toughening obtained in ZnO–ZrO_2 alloys containing equiaxed ZrO_2 ($K_c/K_0 \approx 1.7$) [67] exceeds expections [65] for uniformly spaced equiaxed particles, again suggesting the need for further investigation.

9. COMBINED TOUGHENING MECHANISMS

Numerous factors such as transformation, twinning, microcracking, loss of coherency, etc. can contribute to the energy expenditure causing toughness. The total energy loss from these, including heat generation, must lead to a thermodynamic expression for the toughness. However, a simple summation of all the factors may not be direct or insightful. Insensitivity to certain details arises because the hystersis in the stress–strain curves for the composite material is controlled by the matrix compliance plus the kinetics of transformation and cracking.† Consequently, it is difficult to account for the extent of each contribution in a specific situation. Moreover, it is often immaterial whether the external work and

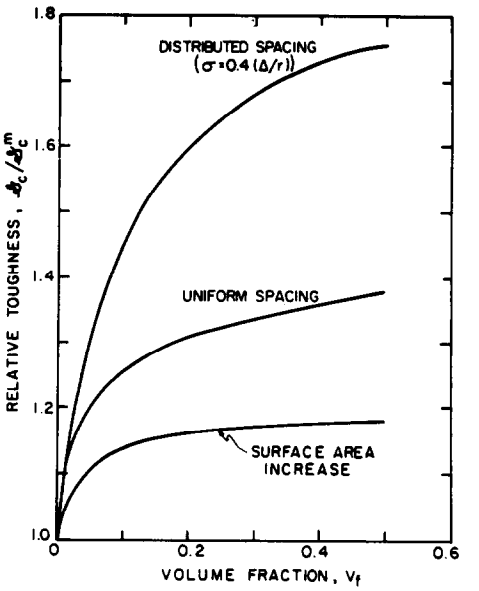

Fig. 40. Relative toughness predictions from crack deflection model for spherical particles including the effect of a distribution in interparticle spacing (Ref. [65]).

chemical forces are dissipated as phonon energy or stored as irrecoverable strain and interfacial energy, unless the net strain or nonlinear zone populations are affected.

Evaluating the importance of various contributions to the toughness is facilitated by two alternate expressions. All the shielding mechanisms can be expressed functionally in terms of K_I relative to the principal crack, as

$$K_c = Y\sqrt{h} + K_{tip}^c \qquad (9.1)$$

where Y depends upon the hysteresis or total crack closure forces. The critical K_{tip}^c includes factors such as deflection or microcrack degradation. Thus, ΔK_c from shielding, expressed in terms of $\sqrt{h}$ is additive with other factors affecting K_{tip}^c.

An alternative expression, based on the relation between h and σ_c, gives insights regarding multiplicative or interactive effects. The pertinent trends can be seen from the supercritical, dilational transformation. For this situation, using an expression analagous to equation (6.10) for h in terms of K_{tip} gives

$$K_c = \left[\frac{0.046\,(1+\nu)\,Ef\varepsilon_{ii}^T}{(1-\nu)\,(\bar{\sigma}_c - \bar{\sigma}_r)} + 1\right] K_{tip}^c \qquad (9.2)$$

where $\bar{\sigma}_r$ is the residual stress in the zone. Thus, it is evident that increasing K_{tip}^c by deflection or degrading it by microcracking has a multiplicative effect through the zone size. For example, crack deflection requires an increase in applied loads in order to bring K_{tip} to the critical level. Consequently, the transformation zone width increases which, in turn, causes additional transformation toughening or microcrack shielding. The basic features are illustrated in Fig. 28.

†As with transformation, a significant proportion of the toughening from microcracking and deflection is associated with irreversible heat flow; in these instances, dissipation ensues after crack segments surmount a deflection or nucleation barrier. Thus, corrections to equation (6.21) for surface roughness or prior cracking at the tip are formally required, but are often smaller than the irreversible heat terms which derive from the conditions for local criticality and the subsequent stress relaxation. Similarly, when deflection is induced by internal stresses, equation (6.25) for $\mathcal{G}_0$, should reflect the relief of residual strain energy near the crack surface. However, the larger factor, Γ, depends on the influence of the internal stresses on the deflection angles and the pertinent criticality relations, equation (8.3), which are as yet unresolved.

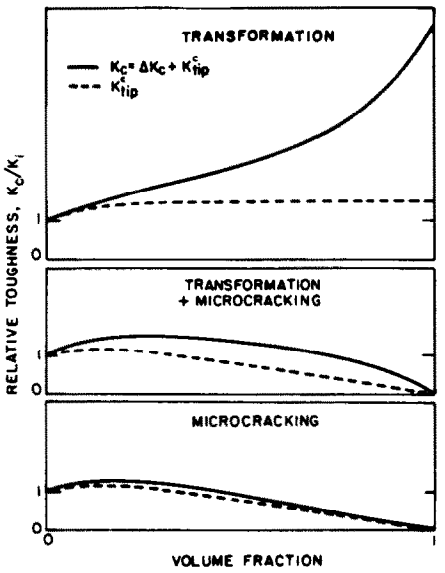

Fig. 41. Schematics illustrating trend of toughness, K_c, with particle concentration comparing shielding by transformation, by transformation plus matrix microcracking, and by matrix microcracking around pretransformed particles. The effects of deflection and matrix microcracking on K_0 are also shown.

A relation for K^c_{tip} which includes deflection effects can be expressed generally as

$$K^c_{tip} = q(\theta, \phi)\, K_i \tag{9.3}$$

where K_i is the intrinsic material toughness and $1/q(\theta, \phi)$ is the reduction in K_{tip} due to deflection (which depends upon particle concentration). A useful, although imprecise, attempt to account for crack tip degradation [equation (7.2)] leads to

$$K_c = \left[\frac{aEf\varepsilon^T_{ii}}{(\bar{\sigma}_c - \bar{\sigma}_r)} + 1\right] q(\theta, \phi)\,(1-f)K_i \tag{9.4}$$

The factor, a, depends upon the balance of transformation and microcracking in the zone.

Schematic curves (Fig. 41) showing the particle concentration dependence on the "asymptotic" K_c implied by equation (6.12), (7.7), (7.8), and (9.4) illustrate the various effects anticipated, under the assumption that the critical stresses to initiate all processes are the same and are independent of particle concentration. The nonlinear trend in transformation toughening with particle concentration arises both from the effect of deflection and because σ_r scales with $fe^T_{ii}E$. The microcrack contribution to toughness is small (or deleterious) when the critical stress is large and transformation shielding develops at large particle concentrations only [Fig. 41(a)], because of the significant microcrack degradation of the crack tip resistance. However, when the critical stress is lower, microcracking can make a positive contribution, at intermediate particle contents [Fig. 41(b)], because the crack tip degradation is minimal.

†This extension was taken to be negligible in Fig. 28.

When microcracking accompanies transformation, the resultant toughness cannot usually be separated into the sum of the two independent contributions either theoretically or experimentally. This behavior obtains because the toughness depends upon the balance of several compensating factors, as revealed by changes in the stress–strain hysteresis (Fig. 32). Specifically, the inelastic strain is increased by microcracking, compared with that for the uncracked-stress-induced-transformation, but the residual stress on the zone is reduced. Furthermore, the net hysteresis area is affected by the relative values of the critical stresses for transformation and microcracking. When the critical stress for microcracking exceeds that for transformation, only a fraction of the transformation zone contributes to microcracking shielding, and the two hysteresis contributions are approximately additive over the appropriate zones. However, the tip degradation, especially at large concentrations, limits both the zone size and the toughening. Conversely, if microcracking occurs at a smaller critical stress, the entire transformation zone experiences microcracking. Moreover, the interaction stresses (Figs 32 and 41), exceed those for microcracking in pre-transformed material. This situation gives the greatest toughening for the combined mechanisms.

Finally, when considering mechanism combinations it is important to recall that the stress induced nonlinearities that cause shielding provide large R-curve effects, because a wake is required to develop the toughness. Conversely, the factors affecting K_{tip} are typically fully developed after a small extension, of the order of the microstructural scale,† (e.g. the particle size). These differences are likely to be reflected in the slope of the R-curve, which develops differently for different mechanism combinations. Furthermore, microcracking and deflection may also stimulate stable crack branching leading to a continual increase in K_c for the macrocrack, even after stable shielding zones are established.

10. COMPARISON WITH EXPERIMENT

10.1. Partially stabilized zirconia

Before embarking on a detailed comparison with experiment, it is important to recognize that the mechanical behavior of PSZ (and other ZrO_2 containing alloys) is more complex than suggested by Fig. 1. One issue is the development of near surface *residual compression*, induced by grinding or sawing. Specifically, the strengths of material containing tetragonal ZrO_2 can be increased by $\gtrsim 20\%$ by machining [1]. Furthermore, the apparent toughness can similarly be increased by machining damage at sawn notches (Fig. 26). Thus, the properties of predominantly tetragonal, underaged, material, reflect a combined effect of transformation induced surface compressive stresses and toughening from transformation shielding and other factors. Another

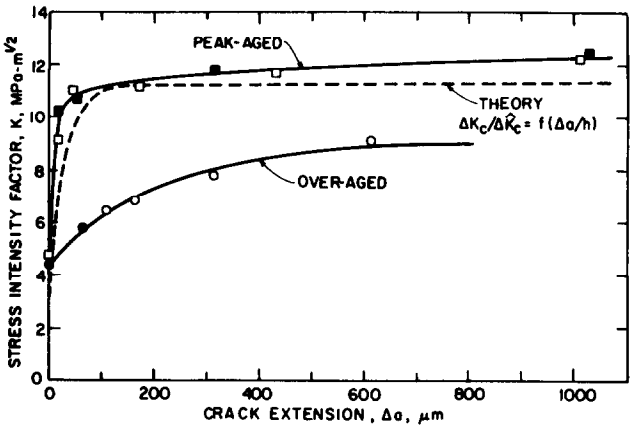

Fig. 42. R-curves for peak-aged MgO/PSZ containing transformable precipitates and for subeutectoidal overaged MgO/PSZ containing extensive grain boundary monoclinic ZrO_2 (Ref. [19]).

significant issue concerns the toughness of the monoclinic, overaged material which serves as the *reference toughness*, K_0. The initial toughness of this material can be more than twice that of single phase cubic material (2 MPa-m$^{1/2}$) [1, 18]. This toughening apparently derives from microcrack shielding, deflection, and branching. A further complexity concerns the significant *R-curve* behavior exhibited by both underaged and overaged material, i.e. increasing toughness with continued propagation. Analysis of most toughness data is ambiguous as a consequence of uncertainties regarding the location on the R-curve. For the explicit comparisons between experimental and theoretical toughnesses which follow, the toughness data selected from the literature were measured from etched, annealed, or carefully polished surfaces. These toughnesses avoid machining effects but may underestimate the asymptotic values. Finally, it is important to appreciate that for all materials, the strengths and toughnesses depend on heat treatment details that affect the intragranular and intergranular precipitates which, in turn, affect the nucleation of the martensite transformation.

It is expedient to assess R-curve behavior before proceeding with other comparisons since the details of the R-curve may influence the measured levels of toughness. R-curves have been measured for a few highly toughened MgO/PSZ materials (Fig. 42) [18, 19]. The large, initial rise in toughness is approximately consistent with that anticipated for transformation shielding (Fig. 14).† The subsequent continual, but slow rise in toughness probably reflects small microcracking and crack branching effects.

†The predicted R-curve for a dilational transformation with a hydrostatic zone front (Fig. 14) is plotted in Fig. 42, assuming a zone width ($h = 17\,\mu$m) indicated by interferometry on the surface (plane stress). Using this h, the initial rate of toughness increase is underestimated, as would be anticipated were the zone front flattened as suggested by Fig. 15.

‡For this and subsequent calculations, $E = 200$ GPa, $\varepsilon_{ii}^T = 0.045$, $\nu = 0.3$ for ZrO_2 and the rule of mixtures value for the elastic constants of ZTA have been used.

R-curves have also been measured for PSZ materials with a high monoclinic phase content (Fig. 42) [18, 19]. Some of these materials exhibit gradually rising toughness with crack extension. This behavior is similar to that found earlier for other coarse grained materials [68], which revealed significant differences in the fracture energy deduced from initiation (~ 50 J/m^2) and work of fracture measurements (~ 200 J/m^2). Fine scale branching and microcracking, revealed by transmission electron microscopy [18], qualitatively support microcracking as a primary toughening and R-curve mechanism in these materials.

The measurements most amenable to comparison with the predicted toughness include determinations of the transformation zone width, h, and the zone profile. Comprehensive measurements of this type have been made for MgO/PSZ and CaO/PSZ by Swain *et al* [6, 69], using X-ray, optical, TEM, and Raman techniques. In these systems, essentially all tetragonal particles within the transformation zone tend to transform. Consequently, the supercritical solutions are deemed most pertinent. The available experimental data are summarized in Fig. 43. Also shown is the supercritical toughness predicted‡ by assuming that only the dilatation contributed to the crack shielding and that the zone profile is dictated by the hydrostatic crack tip field, ΔK_d [equation (6.12)]. Evidently, only about a third to half of the observed toughness is accounted for by this model. The additional toughness may arise from transformation shear contributions, zone shape effects, or other shielding mechanisms. The second line on Fig. 43, denoted ΔK_u or ΔK_{sd}, indicates the nearly identical toughening predicted for a uniaxial transformation strain, ΔK_u [equation (6.19)], or from pure dilation with a zone front bounded by $\pi/3$ shear bands, ΔK_{sd}, [equation (6.15)]. Either transformation mechanism accounts for much of the additional toughening.

To distinguish between these possibilities, appeal is made to transmission electron microscopical observations of particles within the transformation zone.

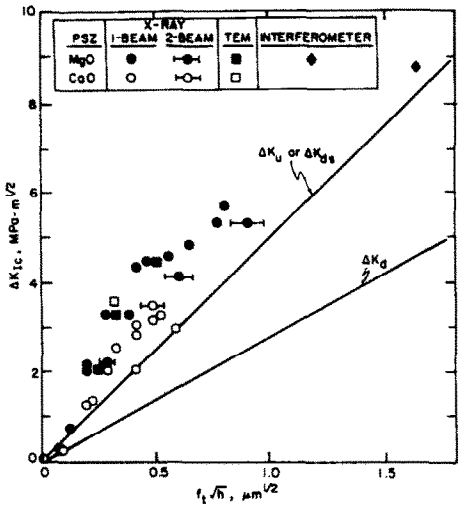

Fig. 43. Comparison of ΔK_c for PSZ with measured transformed zone size and concentration (typically $f = 0.4$).

Specifically, observations in MgO/PSZ (after unloading) reveal that the twins are usually aligned parallel to the plane of the lenticular precipitates and are not preferentially oriented with respect to the crack tip strain field [13, 70]. Such observations are not consistent with a uniaxial transformation strain mechanism, ΔK_u, which would require that the strains be substantially aligned along the principal stress axis of the crack field. The available data are more consistent with a zone shape effect. Specifically, TEM observations on indentation induced cracks indicate that the zone extension in front of the crack is smaller than that expected for a zone determined by the mean stress [13]. Furthermore, preliminary observations made on a PSZ containing a large transformation zone ($h \simeq 16\,\mu$m) suggest that the transformation occurs in shear bands, such that minimal transformation occurs directly in front of the crack [12]. The present shear band estimate of the dilatational toughening, ΔK_{sd}, should, thus, provide the more appropriate basis for comparison with the measured toughness (provided that the zone profile is independent of the zone width, which has not been verified).

Most but not all (i.e. 80% for CaO/PSZ and 60% for MgO/PSZ) of the measured toughness thus appears to be explicable in terms of the dilatation of the particles, subject to a zone shape determined by shear stresses. The additional toughening may be associated either with microcracking (although relatively few microcracks are observed in peak aged material using TEM techniques) or with a partially reversed transformation causing the observed zone width to be smaller than that accompanying crack extension. However, we moderate this conclusion by two cautionary remarks. Firstly, zone fronts other than that bounded by 60° shear bands invariably result in reduced shielding and thus, a lower toughness than given by the present ΔK_{sd} estimate. Secondly, the development of a shear front by autocatalytic transformation implies the existance of an appreciable net shear strain within the band and hence, shear contributions to the toughness that remain to be addressed.

The deflection component of the toughness of PSZ appears in the reference toughness, K_0, and *not* in ΔK_c. Isolating this contribution is difficult. The K_0 taken for the construction of Fig. 43 ($K_0 = 3.2$ MPa-m$^{1/2}$) was somewhat arbitrarily based on the minimum observed toughnesses of overaged and underaged material. In fact, K_0 probably varies during aging and with precipitate type. The toughness of overaged material, being appreciably larger than the value reported for cubic ZrO_2 ($K_c = 2.0$ MPa-m$^{1/2}$), reflects the deflection of the cracks around the monoclinic precipitates (Fig. 39). However, the deflection contribution is likely to be lower for underaged, tetragonal material (Section 8) and to increase with aging, as the monoclinic zone becomes fully established. Also, the higher ΔK_c determined for MgO/PSZ than CaO/PSZ may be an indication of greater deflection around the lens shaped precipitates (and higher actual K_0).

Finally, it is noted that both the strength and toughness of PSZ decrease rapidly with temperature [6, 71] (Fig. 44). Furthermore, the transformation zone width (measured by X-rays on cooled samples) also decreases at elevated temperature [6]. Both factors reveal the anticipated effects of the increase in σ_c with increase in temperature (Section 6.6).

10.2. Zirconia toughened alumina

The interpretation of trends in the toughness and strength of ZTA materials exhibits a greater level of uncertainty than that associated with PSZ. The behavior of these materials indicates complex de-

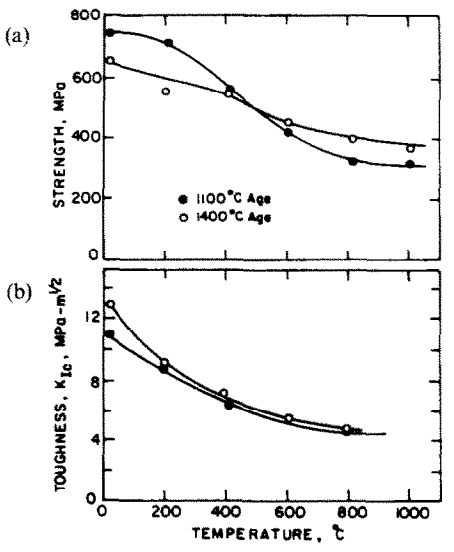

Fig. 44. Temperature dependence of (a) strength and (b) toughness for MgO/PSZ given two different heat treatments (courtesy M. V. Swain).

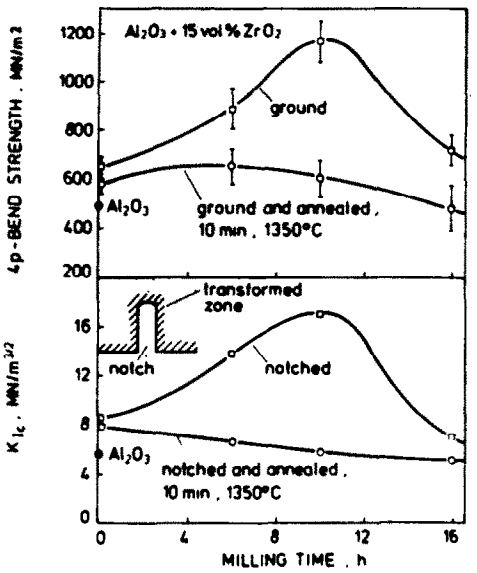

Fig. 45. Flexural strength and fracture toughness of Al_2O_3–15% ZrO_2 alloys made from powder attrition milled for various times to reduce the particle size. Machining-induced transformation is "healed" by the indicated annealing (Ref. [5]).

pendencies including explicit effects of ZrO_2 content, f, indirect effects of f on the critical transformation stress, σ_c, variable contributions of microcrack shielding and degradation, and sometimes dramatic effects of machining induced surface compression [5] (Fig. 45).

Initially, trends with ZrO_2 content are examined. In Al_2O_3–ZrO_2 with a small Y_2O_3 addition, tetragonal ZrO_2 can be retained to high ZrO_2 concentrations (depending upon grain size) [4, 61]. In some systems ΔK_c, when normalized for the modulus differences, increases monotonically (but not quite linearly) with f (Fig. 46) [4]. The strengths also tend to reflect the increases in toughness with f (Fig. 46). The trends are thus broadly consistent with expectations of the models. Conversely, in Al_2O_3–ZrO_2 without stabilizer, as-fabricated materials usually contain some monoclinic phase, with the relative monoclinic content increasing as the ZrO_2 content increases [21, 72]. In these materials, a peak is frequently observed in K_c and strength as shown in Fig. 47 [72]. This peak occurs at a ZrO_2 volume concentration coincident with a substantial increase in the relative monoclinic content in the as-fabricated material. Such behavior suggests an autocatalytic reduction in σ_c with increasing f (although it may also reflect increased ZrO_2 particle sizes). In consequence, the best strengths and toughnesses usually obtain with Y_2O_3 containing materials.

Transformation zones in ZTA exhibit substantial differences from those encountered in PSZ. Specifically, the transformation is inhomogeneous, such that patches of transformed particles exist [22, 28]. Furthermore, the larger, angular particles at the grain junctions preferentially transform. Subcritical transformation conditions thus apply. Transformation induced microcracks are also observed in

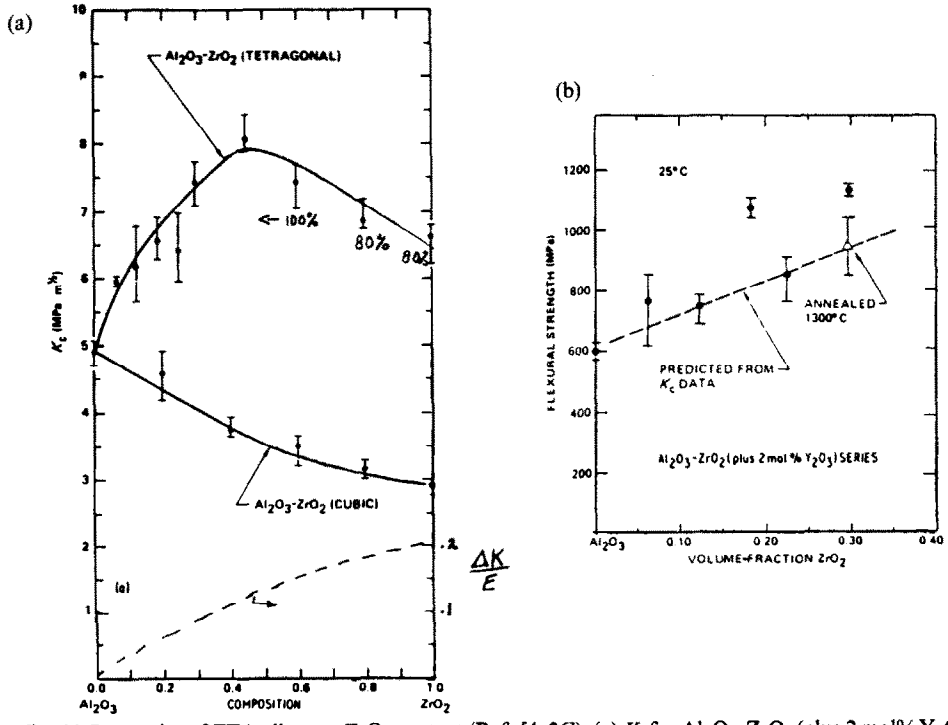

Fig. 46. Properties of ZTA alloys vs ZrO_2 content (Refs [4, 26]): (a) K_c for Al_2O_3–ZrO_2 (plus 2 mol% Y_2O_3) which is primarily tetragonal and for Al_2O_3–ZrO_2 (plus 7.5 mol% Y_2O_3) which is cubic. Also shown is $\Delta K_c/E$ for the tetragonal material taking the cubic toughness for K_0. (b) Flexural strength for the toughened Al_2O_3–ZrO_2 (plus 2 mol% Y_2O_3) materials.

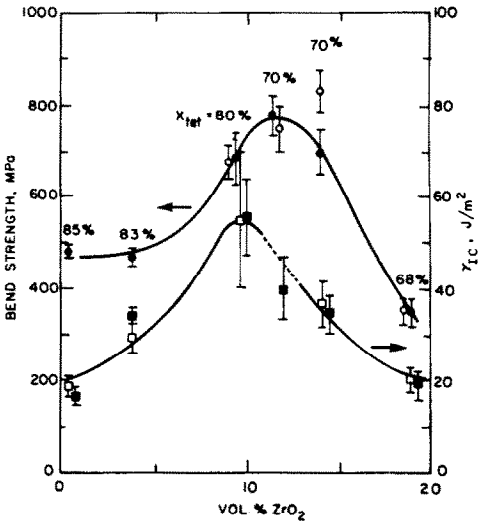

Fig. 47. Dependence of strength and fracture energy for Al_2O_3–ZrO_2 alloys on ZrO_2 content comparing (●) as-machined strength, (○) as-annealed strength, (□) as-annealed DCB fracture energy, and (■) as-mechanically polished, indentation method fracture energy.

some instances [21, 61, 73]. Comparison of experimental measurements with the predictions thus requires detailed determination of the fraction of transformed particles and of microcracks, as a function of distance from the crack plane.

Measurements of the transformed fraction have been conduced on one system during *in-situ* loading in TEM. A diagram showing the spatial distribution of transformed particles after successive extension increments is shown in Fig. 48, and the corresponding

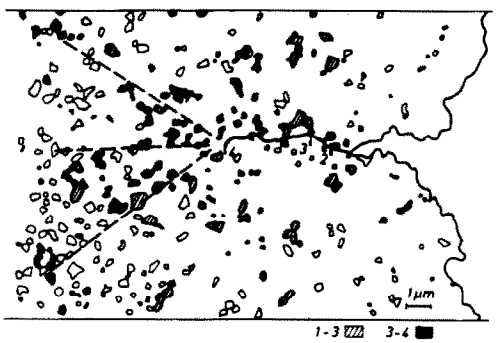

Fig. 48. Schematic representation of transformation zone from *in-situ* TEM experiment on Al_2O_3–15% ZrO_2 materials. The specimen was strained so that the crack successively propagated to different positions (1, 2, 3, 4). All ZrO_2 inclusions are marked on the drawing. Hatched areas: ZrO_2 grains transformed during advance of crack from hole to position 3. Dark areas: ZrO_2 grains transformed during crack extension from position 3 to 4 (courtesy M. Rühle).

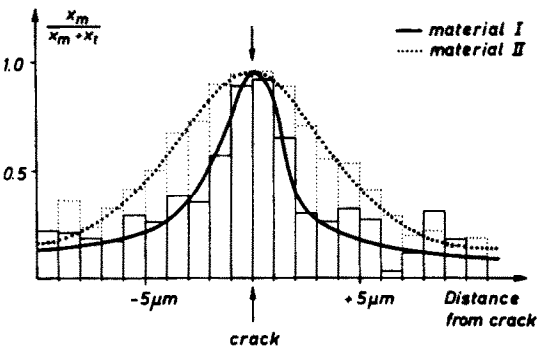

Fig. 49. Fraction of transformed ZrO_2 grains as a function of distance from the crack for Al_2O_3–15% ZrO_2 materials I and II as determined from *in-situ* TEM experiments (courtesy M. Rühle).

distributions of monoclinic phase in the wake are shown [28] for two materials in Fig. 49. For these materials, the spatial variations in the transformation zone at the crack front (Fig. 49) suggest that shear stresses affected transformation. Indeed, determinations of the toughness change for a subcritical, *uniaxial* transformation strain, ΔK_u, (using the results from Fig. 49 in conjunction with equations (6.19) and (6.35), Table 2) account for most of the toughness, assuming that a matrix toughness of 3–4 MPa-m$^{1/2}$ applies. Furthermore, submicron particles of ZrO_2 in Al_2O_3 typically contain one set of parallel twins, with the major dilational strains perpendicular to the twin plane [74]. Consequently, the uniaxial strain postulate would seem plausible. However, it has not yet been shown that the twins tend to align with the stress field when formed around a crack. Final assessment of the role of the uniaxial mechanism awaits further study of crack tip transformations.

The existence of microcrack toughening in ZTA has been indicated by several factors. Microcracking has been identified in Al_2O_3–ZrO_2 materials by microscopy and indicated by low elastic moduli [21, 61]. Large K_c values, up to 10 MPa-m$^{1/2}$, have been obtained for ZTA with 15% ZrO_2 containing primarily monoclinic phase [57]. Such toughnesses cannot be explained by deflection. Strong support for significant microcrack shielding emerges from observations on an exclusively monoclinic, 15% ZrO_2 material [73]. Immediately after cooling from the annealing temperature, this material had a high toughness, $K_c = 11$ MPa-m$^{1/2}$. However, during the ensuing 12 h at room temperature, the toughness decreased (to 5 MPa-m$^{1/2}$), while the modulus also decreased (to 75% of the uncracked value). Such behavior is consistent with the spontaneous development of mi-

Table 2. Calculated toughnesses for subcritical transformations

Material	Measurements K_c (MPa-m$^{1/2}$)	Calculations K_u (MPa-m$^{1/2}$)	K_0 (MPa-m$^{1/2}$)
Al_2O_3–15 vol% ZrO_2 (I)	4.9	1.6	3.3
Al_2O_3–15 vol% ZrO_2 (II)	6.6	2.2	4.4
ZrO_2–3.5 m% Y_2O_3 Polycrystal	6.2	$1.0^{+0.5}_{-0.3}$	$5.2^{+0.3}_{-0.5}$

crocracks that reduce the potential for microcrack shielding and cause the decrease in modulus. However, it is important to appreciate that, except for qualitative observations of increased microcracking around identations, no demonstration or characterization of a shielding zone of increased microcrack density around cracks yet exists.

Recent experimental observations provide support for a *coupled* influence of transformation and microcracking on the toughness of some ZTA materials. One series of experiments demonstrated an apparent insensitivity of K_c to the initial tetragonal phase content [75]. Specifically, systematic variation in the proportion of tetragonal particles up (to 40% monoclinic) for a constant total particle content, 15% (achieved by the thermal transformation of a specific fraction of particles), resulted in an essentially invariant toughness and strength. Combined microcrack and transformation toughening is also suggested by the rapid rise in the toughness with ZrO_2 content observed by Green [21] (Fig. 50). Similar behavior is again indicated by a temperature insensitive K_c for the 9% ZrO_2 material illustrated in Fig. 47 [76].

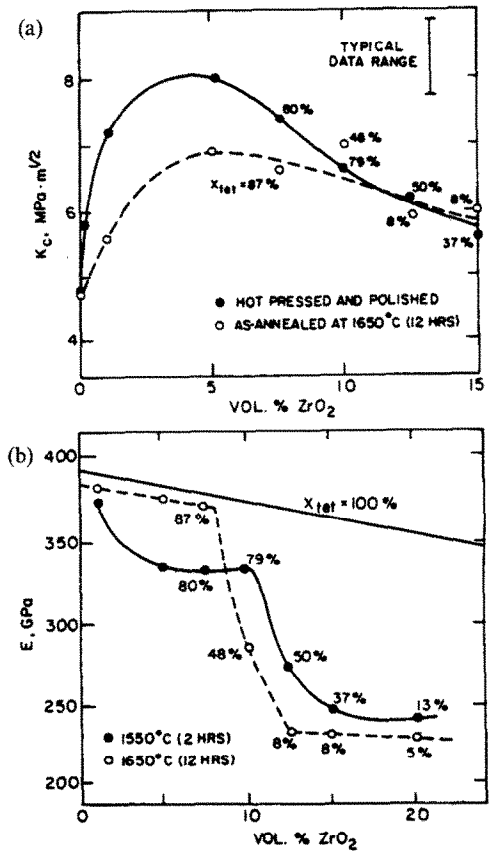

Fig. 50. Toughness and modulus for ZTA materials as a function of ZrO_2 content and extent of prior transformation to monoclinic (Ref. [21]): (a) critical stress intensity factor for undoped materials; (b) Young's modulus illustrating the effects of the lower ZrO_2 modulus for tetragonal material (Y_2O_3-stabilized) and the reduction in modulus from microcracking induced by spontaneous transformation in undoped alloy.

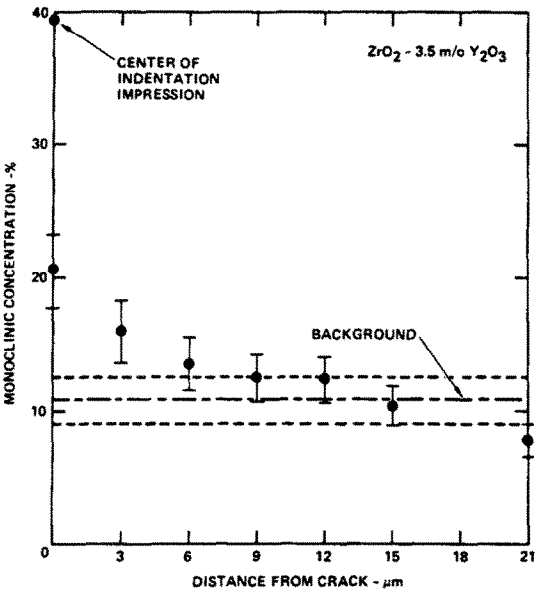

Fig. 51. Monoclinic concentrations as a function of distance from the crack plane as determined by Raman microprobe for a polycrystal with 3.5 mol% Y_2O_3 using an indentation crack (Ref. [56]),

The preceeding discussion indicates that a clear assessment of toughening in ZTA has not yet emerged. Some instances provide strong support for transformation toughening, perhaps involving a uniaxial transformation strain mechanism; others are more supportive of microcrack toughening. Coupled effects also appear in certain materials. Perhaps surprisingly, the highest toughnesses reported to date for ZTA materials with low (<20%) ZrO_2 contents are for materials in which microcracking has been indicated to provide the primary toughening. It thus seems appropriate to conclude that the predominant toughening mechanism in ZTA is material and processing dependent and that each system requires comprehensive study to elucidate the prevailing source of the strength and toughness.

10.3. Tetragonal zirconia polycrystals

Fully tetragonal polycrystals can be retained at room temperature with additions of Y_2O_3 (or rare earth oxides) which lower the driving force for transformation. The behavior of these materials is complicated by the presence of tetragonal material (T′ phase) with high stabilizer content, resulting from the diffusionless transformation of cubic material during cooling. [27, 77]. The latter material is more stable and much more difficult to transform to monoclinic. Single crystals with similar compositions have also been made [78]. Some of these have low Y_2O_3 content tetragonal precipitates in a cubic or T′ matrix. Other crystals may be nearly all T′, often containing a submicron array of antiphase domains and twins [79].

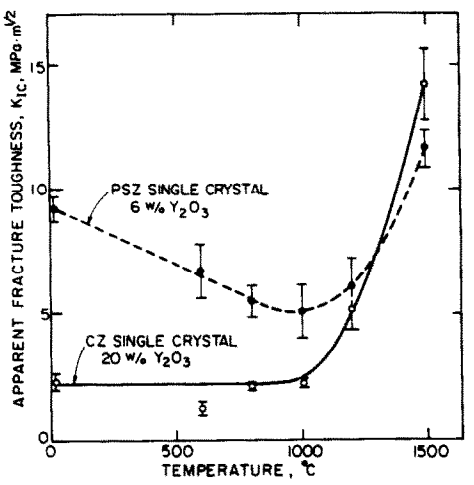

Fig. 52. Fracture toughness as a function of temperature for Y_2O_3/PSZ single crystal containing tetragonal precipitates, and cubic crystal (Ref. [78]).

Toughnesses as high as 9 MPa-m$^{1/2}$ have been reported for tetragonal polycrystals [25, 29] and single crystals [78]. The strengths are also among the highest reported for any transformation toughened materials. The best strengths reportedly exceed 1 GPa with isolated samples up to 2 PGa. The toughness decreases with increases in temperature for both Y_2O_3 stabilized single crystals [78] (Fig. 51) and CeO_2 stabilized polycrystals [80], reflecting the increase in critical stress and the decrease in zone width with decreasing chemical driving force. The toughness and strength similarly decrease with Y_2O_3 content, reflecting a reduction in tetragonal content or an increase in the critical transformation stress [24, 26, 81].

Several measurements, such as recent X-ray data of fracture surfaces [81], indicate that the transformation zone size and the monoclinic population within the zone decrease with increase in Y_2O_3 content. Raman microprobe measurements of the transformation zone about cracks in a polycrystal [56] and a single crystal [27, 82] with 3.5 m/o Y_2O_3 reveal a partially populated residual zone extending several microns from the crack (Fig. 52). Similarly, TEM examination of material around cracks in Y_2O_3 stabilized polycrystals [28] reveals a mixture of transformed, untransformed, and occasional partially transformed grains even for a fully tetragonal sample. Seemingly only a small fraction of the tetragonal material in the zone is transformed, even at the crack plane. Subcritical transformation conditions thus apply. However, the predicted toughness, [using the data in Fig. 52 and equations (6.19) and (6.35)] $\Delta K_u \simeq 0.5$–1 MPa-m$^{1/2}$ (Table 2), is significantly below the value $\Delta K_c \simeq 4.2$ MPa-m$^{1/2}$, implied by the measured toughness. This disparity is attributed to transformation *reversal*, as discussed below.

Behavior indicative of transformation reversal has emerged from studies of CeO_2 doped samples with relatively high toughness, $K_c \sim 5$–7 MPa-m$^{1/2}$, and strength, 900 MPa [27, 83]. These samples, containing 15–18% CeO_2, are fully tetragonal: as sintered, after crushing and cooling in liquid nitrogen, and after surface grinding. Further, the fracture surfaces are revealed to be tetragonal upon X-ray, Raman microprobe, and TEM examination. Evidence of stress induced transformation is only attained around hardness indents, where the residual stress allows the monoclinic phase to be retained. The high toughnesses and exceptionally rough fracture surfaces (Fig. 53) indicate these materials are transformation toughened, but that the transformation reverses upon unloading (passage of the crack).

Finally, it is noted that the toughest TZP materials do not exhibit the highest strengths [24, 29]. This trend may be related to grain size affects wherein the high strengths relate to fine grain sizes, which limit the processing related flaw size. Alternatively, slip limited failure (Fig. 4) could account for the behavior of the higher toughness (lower σ_c) materials.

10.4. General trends

The highest reported toughnesses (e.g. 15 MPa-m$^{1/2}$) have been obtained for materials containing

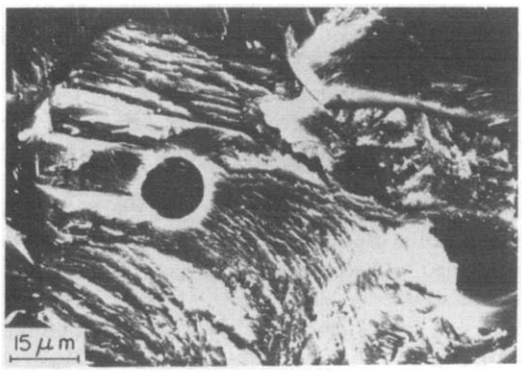

(a)

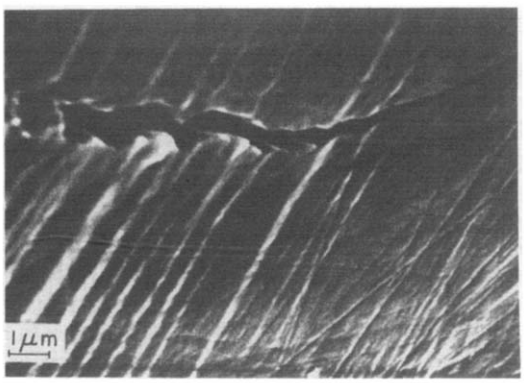

(b)

Fig. 53. SEM micrographs of a tetragonal ZrO_2–18 mol% CeO_2 polycrystal showing: (a) rough fracture surfaces from flexural test, and (b) polished surface containing indentation induced crack which exhibits surface roughening and crack deflection (courtesy T. W. Coyle).

primarily tetragonal ZrO_2, but having a low critical stress [19, 24, 71]. These materials can be significantly strengthened both by machining induced compressive stresses and by transformation toughening. For Al_2O_3–ZrO_2 materials, the highest strengths and toughnesses have been obtained with small Y_2O_3 additions [4, 26, 61]. The additive may be helpful in preventing premature transformation. Both PSZ and ZTA have been made which are primarily monoclinic but exhibit appreciable toughness owing to microcracking and deflection. The toughness in these cases does not usually contribute to the initial strength, but may be beneficial for arrest and retained strength (e.g. for thermal shock resistance) [1, 18, 57]. For both transformation and microcrack toughening, significant R-curve behavior is indicated [18, 19, 71]. The R-curves are initially much steeper for the transformation toughened materials. Asymptotic toughnesses achieved with microcracking occasionally approach those of good tetragonal materials. However, alloys containing appreciable monoclinic phase are susceptible to spontaneous microcracking, which degrades both strength and toughness.

Consideration of all the results suggests that the behavior of the various materials depends qualitatively upon the chemical driving force which, in turn, depends upon undercooling and alloy additions. For highly undercooled materials, which have small particle sizes to inhibit nucleation, the transformation evidently occurs in bursts within particles, once the critical stress, σ_c, is exceeded. In such highly undercooled materials, it has been assumed that nucleation occurs at low enough average stresses that the internal structure largely compensates the net shear stresses or the random orientations average them out. Then, the toughness would be largely determined by dilational strains, plus effects of crack deflection. However, in all cases analyzed herein, additional contributions from deviatoric strains arising from zone shape effects and possibly longer range, net transformation strains have been indicated but not substantiated. At smaller undercoolings, the transformation occurs at higher average stresses. Then, stress coupling is clearly more likely to influence the martensite orientations and internal structure within the transformed particles. Such effects increase the coefficient in the $\Delta K - \sqrt{h}$ relation, which partially compensates the reduction in h. At very small undercoolings the transformation may fully reverse after passage of the crack. Fully reversed transformation may account for the toughness at higher temperatures in MgO/PSZ (Fig. 44) and the Y_2O_3 stabilized single crystals [78] (Fig. 51). In the latter materials, significant toughness is retained at temperatures in excess of the equilibrium temperature ($\sim$500–600°C).†

†The minimum toughness at $\sim$1000°C may occur as the reversible transformation induced toughness and plasticity effects intersect in relative importance.

10.5. Optimum materials

Microstructural and compositional optimization depends upon several interacting factors, as well as application requirements, such as load duration and the range of exposure temperatures and environments. Maximum strength results when the critical stress is low enough to give the widest possible transformation zone without incurring one of three limitations. Each limit results from nearly spontaneous transformation at low stresses. Optimum *toughness* occurs when h is large, but still small relative to the sample size. Thus, the highest attainable toughness occurs at a small but finite critical stress, Fig. 28. The optimum *strength* may be limited by shear band propagation which initiates cracks as in Fig. 4. Both limitations may be related, because shear band formation may result from growth of a transformation zone initiated at a large flaw. Alternatively, strength may be limited by transformation and microcracking around isolated large particles or particle clusters. Strength limiting microcracks around large particles may form spontaneously or at low stress, depending upon the stress to activate the most easily transformed particles. Then, the strength depends upon the steepness of the transformation probability function as well as the flaw population that controls microcracking around the largest particles. For application at a specific temperature, the highest strength and toughness may result from a narrow particle size distribution. However, such distributions may detract from the strength and toughness at other temperatures.

Both PSA and ZTA materials having suboptimal toughness exhibit strengthening that tends to vary with K_c. In contrast, several observations indicate that the strongest materials have less than maximum toughness. This paradox may derive from the aforementioned transformation induced flaw generation. It may also reflect a relative insensitivity to flaw size for highly toughened materials arising from the R-curve behavior and the requisite large flaws at the fracture criticality.

Materials with a small chemical driving force and associated larger critical stress σ_c offer the advantage of having negligible amounts of spontaneously transformed materials which could cause degradation. Such materials can exhibit appreciable toughness even when T is $\geq T_0$ owing to stress induced transformation which may significantly reverse upon unloading. In these instances, the transformation zone may be partially transformed and comprised of martensite plates or shear bands nucleated at the crack tips.

Microcrack toughened materials are reportedly preferable under some conditions, e.g. thermal shock, where high retained strength is important. The toughest materials probably result from combined transformation and microcrack toughening. A clear prescription for optimizing such materials has not yet emerged.

11. CONCLUDING REMARKS

A major impression conveyed by the present article is that a reasonable understanding of transformation toughening has emerged, based upon independent measurements which verify the relationship between increased toughness and transformation zone width. This impression is reinforced by observations of substantial R-curve behavior and of a toughness that increases to a maximum with increased chemical driving force (as influenced by cooling or alloying). However, the implied agreement between theory and experiment has required that certain effects be invoked, without appreciable experimental validation. These effects include: a shear influenced transformation zone profile, partial reversibility of the stress induced transformation and limited shear coupling with the crack tip stress field. Systematic investigation of these effects constitutes an important topic for further study.

The prediction of the transformation zone width and the strong particle size dependence of the zone width and resultant toughness represent substantially more contentious issues, at least on the basis of present knowledge. The zone width is dictated by the transformation stress which, in turn, is usually determined by the stress induced nucleation criterion. Quantitative knowledge of the nucleation process and the particle size dependence thereof is not presently available. However, general ideas associated with thermal and elastic mismatch induced stress concentrations at facet corners, coupled with preliminary probabilistic considerations, represent a useful basis for further investigation.

Indications exist that imply a role of microcracking in the toughening of certain ZTA and PSZ materials. Preliminary theoretical models of the specific role of microcracks are now available, but direct evidence of a discrete microcrack zone has not been obtained in any instance. Clearly, before microcrack toughening can be accorded serious consideration, the microcrack zone must be identified. Methods based on X-ray (or neutron) absorption may be pertinent. Comparison between theory and experiment may then proceed, as exemplified by the progress achieved for transformation toughening.

Experimental studies of the crack path in toughened materials frequently indicate appreciable crack deflection. However, deflection theories (although successful in explaining behavior in other systems) have not been able to adequately account for the measured levels of toughness. Consequently, there appears to be scope for further study of deflection toughening, with emphasis placed on the influence of residual strain fields around transformed regions on the deflection process.

Finally, certain trends in the strength of ZrO_2 toughened materials have been proposed, again based on minimal experimental evidence. In particular, a limit on the strength of high toughness materials has been proposed, due to plasticity (transformation shear banding) initiated microcracking. This limit has obvious implications for the design of optimal materials. *In-situ* optical and scanning electron microscopical observations of the shear bands and cracks are needed to develop this concept. In high toughness materials, isolated large ZrO_2 particles have also been identified as strength limiting, due to their propensity to spontaneously transform and induce microcracks. The behavior of large particles thus represents another topic for further investigation.

Acknowledgements—This work was supported by the Office of Naval Research, Contract N00014-81-K-0362 and by the Director, Office of Energy Research, Office of Basic Energy Sciences, Materials Sciences Division of the U.S. Department of Energy under Contract No. DE-AC03-76SF00098. The authors gratefully acknowledge N. Claussen, T. W. Coyle, A. H. Heuer, J. W. Hutchinson, J. C. Lambropoulos, M. Rühle, and M. V. Swain, for helpful comments and for providing unpublished data or manuscripts.

GENERAL BIBLIOGRAPHY

A. H. Heuer and L. W. Hobbs (editors) *Science and Technology of Zirconia, Adv. in Ceram.*, Vol. 3, 475 pp. Am. Ceram. Soc., Columbus, Ohio (1981).

N. Clauseen, M. Ruhle and A. H. Heuer (editors) *Proc. 2nd Int. Conf. on Science and Technology of Zirconia, Adv. in Ceram.*, Vol. 11. Am. Ceram. Soc., Columbus, Ohio (1984).

R. C. Bradt, A. G. Evans, D. P. H. Hasselman and F. F. Lange (editors) *Fracture Mechanics of Ceramics*, Vol. 6, pp. 255–421. Plenum, New York (1983).

Aaronson H. I., Laughlin D. E., Sekerka R. L. and Wayman C. K. (editors) *Proc. Int. Conf. Solid-Solid Phase Transformations*, 1610 pp. T.M.S.-A.I.M.E. Warrendale, Pa.

REFERENCES

1. R. C. Garvie, R. J. H. Hannink and C. Urbani, *Ceramurg. Int.* **6,** 19–24 (1980).
2. D. L. Porter and A. H. Heuer, *J. Am. Ceram. Soc.* **60,** 183–84 (1977).
3. F. F. Lange, *J. Mater. Sci.* **17,** 255 (1982).
4. F. F. Lange, *J. Mater. Sci.* **17,** 247 (1982).
5. N. Claussen and M. Ruhle, *Adv. Ceram.* **3,** 137 (1981).
6. M. V. Swain, R. H. Hannink and R. C. Garvie, *Fract. Mech. Ceram.* **6,** 339 (1983).
7a. R. J. H. Hannink, *J. Mater. Sci.* **13,** 2487 (1978).
7b. R. J. H. Hannink, K. A. Johnston, R. T. Pascoe and R. C. Garvie, *Adv. Ceram.* **3,** 116 (1981).
8. R. C. Garvie, R. J. H. Hannink and R. T. Pascoe, *Nature* **258,** 703 (1975).
9. R. M. McMeeking and A. G. Evans, *J. Am. Ceram. Soc.* **65,** 242 (1982).
10. B. Budiansky, J. W. Hutchinson and J. C. Lambropoulos, *Int. J. Solids Struct.* **19,** 337 (1983).
11. D. Larsen and J. W. Adams, *IITRI Tech. Rep.* **12,** (1982).
12. M. V. Swain, *J. Am. Soc.* In press.
13. L. H. Schoenlein and A. H. Heuer, *Fract. Mech. Ceram.* **6,** 309 (1983).
14. D. L. Porter and A. H. Heuer, *J. Am. Ceram. Soc.* **62,** 298 (1979).
15. A. H. Heuer, *Adv. Ceram.* **3,** 98 (1981).
16. E. C. Subbarao, *Adv. Ceram.* **3,** 1 (1981).

17. W. M. Kriven, W. L. Fraser and S. W. Kennedy, *Adv. Ceram.* **3,** 82 (1981).
18. M. V. Swain, *Fract. Mech. Ceram.* **6,** 355 (1983).
19. M. V. Swain and R. J. H. Hannink, *Adv. Ceram.* 11 (1984).
20. A. H. Heuer, N. Claussen, W. M. Kriven and M. Ruhle, *J. Am. Ceram. Soc.* **65,** 642 (1982).
21. D. J. Green *J. Am. Ceram. Soc.* **65,** 610 (1982).
22. M. Rühle and W. M. Kriven, *Ber. Bunsenges Phys. Chem.* **87,** 222 (1983).
23. W. M. Kriven, *Adv. Ceram.* **3,** 168 (1981).
24. T. Masaki, Toray Co. Ltd. Personal communication.
25. T. K. Gupta, F. F. Lange and J. H. Bechtold, *J. Mater. Sci.* **13,** 1464 (1978).
26. F. F. Lange *J. Mater. Sci.* **17,** 240 (1982).
27. T. W. Coyle, Ph.D. Thesis, M.I.T. Cambridge, Mass.
28. M. Rühle, A. Strecker, D. Waidelich and B. Kraus, *Adv. Ceram.* **11,** 256 (1984).
29. M. Rühle, N. Claussen and A. H. Heuer, *Adv. Ceram.* **11,** 352 (1984).
30. G. T. Hahn, B. L. Averbach, W. S. Owen and M. Cohen, in *Fracture* (edited by B. L. Averbach, D. K. Felbeck, G. T. Hahn and D. A. Thomas), pp. 91–116. Wiley, New York.
31. B. R. Lawn and T. R. Wilshaw, *Fracture of Brittle Solids.* Cambridge Univ. Press (1975).
32. Y. Fu, A. G. Evans and W. Kriven, *J. Am. Ceram. Soc.* **67,** 626 (1984).
33. J. W. Hutchinson, *Non-Linear Fracture Mechanics.* Tech. Univ. of Denmark (1979).
34. D. B. Marshall, M. Drory and A. G. Evans, *Fract. Mech. Ceram.* **6,** 289 (1983).
35. D. Green *J. Am. Ceram. Soc.* **66,** 178 (1983).
36. A. G. Evans, N. Burlingame, M. Drory and W. M. Kriven, *Acta metall.* **29,** 447 (1981).
37. J. D. Eshelby, *Proc. R. Soc.* **A241,** 376 (1957).
38. J. W. Christian, *The Theory of Transformations in Metals and Alloys,* Part I, p. 457. Pergamon Press, Oxford (1975).
39. R. M. Cannon, and T. W. Coyle, *Am. Ceram. Soc. Bull.* **63,** 453 (1984).
40. M. D. Huang and A. G. Evans, *Actal metall.* In press.
41. G. B. Olson and M. Cohen, in *Proc. Int. Conf. on Solid–Solid Phase Transformations* (edited by H. I. Aaronson *et al.*), pp. 1145–1164. T.M.S.-A.I.M.E., Warrendale, Pa (1982).
42. I.-W. Chen and Y.-H. Chiao, *Acta metall.* **31,** 1627 (1983).
43. A. G. Evans, *Acta Met* **26,** 1845 (1978).
44. D. R. Clarke, *Acta metall.* **28,** 913 (1980).
45. S. Schmauder, W. Mader and M. Rühle, *Adv. Ceram.* **11,** 251 (1984).
46. J. R. Matthews, F. A. McClintock and W. Shack, *J. Am. Ceram. Soc.* **59,** 304 (1976).
47. S. B. Batdorf, *Fract. Mech. Ceram. ibid.* **3,** 1 (1978).
48. E. Gumbel, *Statistics of Extremes.* Columbia Univ. Press (1958).
49a. G. B. Olson and M. Cohen, *Scripta metall.* **11,** 345 (1977).
49b. R. J. Salzbrenner and M. Cohen, *Acta metall.* **27,** 739 (1979).
50. J. C. Lambropoulos, Harvard Univ. Report MECH 55 (1984).
51. J. W. Hutchinson, Harvard Univ. Report DEAP 58 (1974).
52. D. B. Marshall, A. G. Evans, B. T. Khuri-Yakub and G. S. Kino, *Proc. R. Soc.* **A385,** 461 (1983).
53. S. J. Burns and R. J. Seyler, *Adv. Ceram.* **11,** 213 (1984).
54. A. G. Evans, *Adv. Ceram.* **11,** 193 (1984).
55. T. W. Coyle and R. M. Cannon, *Am. Ceram. Soc. Bull.* **60,** 377 (1981).
56. D. R. Clarke and F. Adar, *J. Am. Ceram. Soc.* **65,** 284 (1982).
57. N. Claussen, J. Steeb and R. F. Pabst, *Am. Ceram. Soc. Bull.* **56,** 559 (1977).
58. A. G. Evans and K. T. Faber, *J. Am. Ceram. Soc.* **67,** 255 (1984).
59. J. W. Hutchinson. To be published.
60. F. F. Lange, *Fract. Mech. Ceram.* **1,** 20 (1974).
61. P. F. Becher and V. J. Tennery, *Fract. Mech. Ceram.* **6,** 383 (1983).
62. G. C. Sih, *Handbook of Stress Intensity Factors.* Lehigh Univ Press (1974).
63. B. Budiansky and J. O'Connell, *Int. J. Solids Struct.* **12,** 81 (1976).
64. K. T. Faber, *Adv. Ceram.* **11,** 293 (1984).
65. K. T. Faber and A. G. Evans, *Acta metall.* **31,** 565 (1983).
66. T. K. O'Brien, *ASTM STP* **775,** 140 (1982).
67. H. Ruf and A. G. Evans, *J. Am. Ceram. Soc.* **66,** 328 (1983).
68. D. J. Green, P. S. Nicholson and J. D. Embury, *J. Am. Ceram. Soc.* **56,** 619 (1973).
69. R. C. Garvie, R. H. J. Hannink and M. V. Swain, *J. Mater. Sci. Lett.* **1,** 437 (1982).
70. L. H. Schoenlein, A. H. Heuer and M. Ruhle, *Adv. Ceram.* **11,** 275 (1984).
71. L. Li and R. F. Pabst, *Fract. Mech. Ceram.* **6,** 371 (1983).
72. P. F. Becher, *J. Am. Ceram. Soc.* **64,** 37 (1981).
73. N. Claussen, R. L. Cox and J. S. Wallace, *J. Am. Ceram. Soc.* **65,** 190 (1982).
74. W. M. Kriven, *Adv. Ceram.* **11,** 425 (1984).
75a. N. Claussen and M. Ruhle, private communication.
75b. R. Lindemann, Ph.D. thesis, Univ. of Stuttgart (1985).
76. P. F. Becher and C. C. Wu, *Am. Ceram. Soc. Bull.* **59,** 37 (1980).
77. V. Lanteri, T. E. Mitchell and A. H. Heuer, *Adv. Ceram.* **11,** 118 (1984).
78. R. P. Ingel, D. Lewis, B. A. Bender and R. W. Rice, *J. Am. Ceram. Soc.* **65,** 150 (1982); *Adv. Ceram.* **11,** (1984).
79. D. Michel, L. Mazerolles and M. Perez y Jorba, *Adv. Ceram.* **11,** 131 (1984).
80. C. A. Andersson and T. K. Gupta, *Adv. Ceram.* **3,** 184 (1981).
81. M. V. Swain, private communication.
82. T. W. Coyle, R. M. Cannon, M. Bell and C. Needham, *Am. Ceram. Soc. Bull.* **62,** 377 (1983).
83. T. W. Coyle, W. S. Coblenz and B. A. Bender, *J. Am. Ceram. Soc.* To be published.